

Floquet-engineered Emergent Massive Nambu–Goldstone Modes

Yang Hou,¹ Zhanpeng Fu,² Roderich Moessner,³ Marin Bukov,³ and Hongzheng Zhao^{1,*}

¹*School of Physics, Peking University, 100871 Beijing, China.*

²*Zhiyuan College, Shanghai Jiao Tong University, 200240, Shanghai China*

³*Max Planck Institute for the Physics of Complex Systems, Nöthnitzer Str. 38, 01187 Dresden, Germany.*
(Dated: September 4, 2024)

We present a general framework to implement massive Nambu–Goldstone quasi-particles in driven many-body systems. The underlying mechanism leverages an explicit Lie group structure imprinted into an effective Hamiltonian that governs the dynamics of slow degrees of freedom; the resulting emergent continuous symmetry is weakly explicitly broken, giving rise to a massive Nambu–Goldstone mode, with a spectral mass gap scaling linearly with the drive period. We discuss explicit and experimentally implementable realizations, such as Heisenberg-like spin models that support gapped spin-wave excitations. We provide a protocol to certify the existence of the massive Nambu–Goldstone mode from the dynamics of specific observables, and analyse the dispersion spectrum and their lifetime in the presence of weak explicit symmetry breaking.

Introduction.— Collective excitations in many-body systems are a long-standing yet everlasting subject. Among others, of particular importance are massless Nambu–Goldstone modes (NGs) appearing due to spontaneous breaking of a continuous symmetry [1]. They are essential for understanding various intriguing many-body phenomena, e.g., superfluidity and phonons in crystals [2]. Yet, most symmetries in realistic systems are indeed only approximate. The interplay between explicit symmetry breaking (SB) and spontaneous symmetry breaking (SSB) can generate massive Nambu–Goldstone modes (mNGs) [3–5], e.g., the π -meson.

Over the past decades, properties of mNGs have been extensively investigated in equilibrium [6–36], including, e.g., counting rules of their numbers [2], mass [9, 11] and damping processes [24, 28]. In contrast, little has been known in the case of generic time-dependent systems, which are ubiquitous in nature and experiments. Perhaps one of the simplest setups are time-periodic (Floquet) systems, which have been recently proposed as a toolbox to realize a zoo of novel non-equilibrium phases of matter [37–55]. Yet, the very existence of mNGs in Floquet systems remains largely unexplored, especially when symmetries are not exact. Here, we pose the questions of whether one can exploit Floquet protocols to manipulate various explicit SB processes [56, 57], stabilize mNGs, and even engineer intriguing non-equilibrium features without a counterpart in static systems.

For many physical systems explicitly fine-tuning SB process is a fundamental challenge as it normally occurs beyond our control, like defects or impurities in materials. Therefore, we mostly consider engineered quantum platforms that allow for the simulation of time-dependent systems in idealized and controlled settings [58–61].

In this work, we build on the Floquet framework to explore whether or not, and under which conditions, one can implement emergent mNGs; we investigate how to

tune their fundamental properties, such as mass and lifetime, even when the drive protocol does not preserve any symmetry. Realizing such a control scheme is a demanding challenge since: (1) The existence of mNGs in equilibrium requires a well-defined SSB ground state w.r.t. a continuous symmetry; however, generic Floquet protocols break all symmetries, and the concept of SSB and its implications become elusive; (2) How to certify the existence of the mNGs from the experimentally accessible dynamical signatures remains unclear. (3) Due to the absence of energy conservation, driven systems eventually heat up to an infinite temperature ensemble, obliterating any non-trivial collective behavior.

To address these challenges, we construct a Floquet protocol that leads to emergent mNGs with a parametrically tunable gap size and lifetime. The key conceptual ingredient is a driving scheme that dynamically exhibits an emergent hierarchical symmetry structure [56], together with a Lie group structure that guarantees the appearance of mNGs. The construction applies to classical and quantum systems alike, irrespective of the underlying microscopic details. Due to prethermalization-induced suppression of energy absorption at large drive frequencies (compared to local energy scales) [62–64], emergent mNGs can be identified well before the onset of heating. Moreover, we show that they respond differently to various types of explicit SB perturbations: their mass originates from effective processes preserving a subgroup structure, while their lifetime is determined by even weaker effects that eventually break all symmetries.

As a concrete demonstration, we apply our protocol to a classical many-body spin system where NGs correspond to magnon (or spin-wave) excitations. To leading order in the drive period T , the dynamics is captured by the ferromagnetic (FM) Heisenberg model with a continuous $O(3)$ symmetry; this symmetry degrades to $O(2)$ by a weak effective magnetic field along the z -axis, opening up a magnon excitation gap that scales linearly with T . We perform large-scale and long-time numerical simulations to verify the existence of mNGs from the non-equilibrium dynamics of observables; in particular, we

* hzhao@pku.edu.cn

find a quantitative agreement in the excitation spectra obtained numerically from the dynamical structure factor (DSF) and analytically using spin-wave theory. Similar dynamical signatures also occur in quantum systems, and hence can be used as a practical diagnostic of mNGs in experiments with quantum simulators.

Drive-induced higher-order processes break the $O(2)$ symmetry and destabilize the mNGs, leading to characteristic oscillations in quasi-conserved quantities, e.g., the $x/y/z$ components of the total magnetization. Their amplitudes exhibit distinctive scaling behavior, $A_{x/y} \propto T$ and $A_z \propto T^2$, confirming the hierarchical breakdown of the $O(3)$ symmetry in time. Despite their eventual heat death, these mNGs exhibit a parametrically long lifetime: the linewidth of the DSF scales as $\Gamma \propto T^3$ with a scaling exponent different from the naive Fermi's Golden rule expectation. We justify it by applying a recently developed hydrodynamic theory designed to address the limit of weak explicit SB [24], as is the case in the high-frequency regime. As Γ is much smaller than the gap size, drive-induced mNGs constitute well-defined quasi-particles of the Floquet system in the high-frequency regime.

Protocol.— We start by introducing the driving protocol which involves piece-wise constant Hamiltonian evolution. The Floquet operator reads

$$U_F = U_0^- U_1^- U_0^+ U_1^- U_2 U_1^+ U_0^- U_1^+ U_0^+ U_2, \quad (1)$$

$U_0^\pm = e^{\pm i H_0 T'}$, $U_1^\pm = e^{\pm i H_1 T'/2} e^{\pm i H'_1 T'/2}$, $U_2 = e^{-i H_2 T'}$, where $T' = T/10$ is the evolution time for each step and T is the total drive period. To understand the resulting dynamics, one can define a static effective Hamiltonian Q through the relation $U_F \equiv e^{-i Q T}$. In the high-frequency regime, one can perturbatively determine $Q = \sum_m Q^{(m)}$, with $Q^{(m)} \sim T^m$, and its truncation at a finite order can be used to approximate the stroboscopic time evolution. Using an inverse-frequency expansion we obtain the two lowest order contributions

$$Q^{(0)} = \frac{1}{5} H_2, \quad Q^{(1)} = -\frac{iT}{200} ([H_1, H'_1] + 2[H_1 + H'_1, H_2]), \quad (2)$$

and H_0 only appears in higher-order terms.

In general, mNGs can be implemented by this protocol if $Q^{(0)}$ has a continuous symmetry. Yet, here we specifically require that $Q^{(0)}$ preserves one non-Abelian symmetry group, G_2 , such that one can separately tune the mass and lifetime of mNGs by different higher-order processes, as elaborated below. For generic drives the first-order correction $Q^{(1)}$ breaks all subgroups of G_2 . However, one can use the following construction to break the symmetry hierarchically. An illustrative case is when H_1 and H'_1 are proportional to two non-commuting generators of G_2 , say X_i and X_j . Denoting the non-vanishing structure constants as c_{ijk} , with $[X_i, X_j] = \sum_k c_{ijk} X_k$, allows us to write $Q^{(1)}$ as a superposition $Q^{(1)} = \mu \sum_k c_{ijk} X_k \equiv \mu M$ where μ denotes the chemical potential [65]. Consequently, $Q^{(0)} + Q^{(1)}$ preserves a subgroup $G_1 \subset G_2$, spanned by the generators

that commute with M . Suppose $|0\rangle$ labels the ground state of $Q^{(0)} + Q^{(1)}$ and the generator M is broken (either explicitly or spontaneously). Ref. [66] has proved that generators that commute with M can generate standard massless NGs, but non-commuting generators necessarily excite mNGs; the corresponding masses, exactly determined by group theory, are proportional to the chemical potential. In this example, μ , and therefore the mass of the emergent mNGs, is linear in T .

Since we do not assume any further symmetry structure in H_0 , the symmetry group G_1 will be degraded to the trivial group by the next-order (in T) term $Q^{(2)}$. Therefore, although both explicit SB and SSB are allowed by the effective Hamiltonian $Q^{(0)} + Q^{(1)}$, only explicit SB occurs in the exact Floquet protocol. This is of significant importance when seeking quantitative descriptions of mNGs and two possible scenarios need to be addressed separately: $|0\rangle$ is non-degenerate (Case 1) or degenerate (Case 2), w.r.t. the symmetry G_1 .

In Case 1, $|0\rangle$ is unique and independent of T , and $Q^{(2)}$ slightly perturbs it by a negligible amount. Hence, $Q^{(0)} + Q^{(1)}$ is sufficient to predict the masses and dispersion of the mNGs to a good approximation. Case 2 is more subtle since $Q^{(2)}$ breaks G_1 and lifts the degeneracy; hence, one has to take at least $Q^{(2)}$ into account to determine the new ground state [67]. For simplicity, in the following, we focus on Case 1 and briefly comment on Case 2 in the end; additional discussions are presented in the Supplementary Material (SM).

Higher corrections of order $O(T^2)$ also lead to a finite lifetime of mNGs at any finite T ; however, their influence can be systematically pushed to later times by increasing the driving frequency.

The proposed construction is generic as it relies only on the aforementioned group structure; in particular, it is independent of the microscopic details of the drive, and hence can be applied to various physical systems of interest. The piece-wise constant protocol Eq. (1) can be implemented, e.g., on gate-based digital quantum simulators [60, 68]; in the SM we also present a continuous drive feasible for analog quantum platforms [59, 69–71].

Effective Description.— This construction applies equally to quantum and classical systems. In the latter, the derivation of the effective Hamiltonian can be obtained by replacing the commutator $-i[\cdot, \cdot]$ in Eq. (2) with the Poisson bracket $\{\cdot, \cdot\}$ [72]. Hence, to verify the existence and properties of mNGs, especially the ones at a long wavelength, we focus on a 1D classical spin chain with spin-wave excitations, for which the long-time and large-size numerical simulation can be efficiently implemented [73–77]. We consider the Hamiltonians

$$\begin{aligned} H_2 &= -J_2 \sum_j \mathbf{S}_j \cdot \mathbf{S}_{j+1}, \quad H_1 = -h_x \sum_j S_j^x, \\ H'_1 &= -h_y \sum_j S_j^y, \quad H_0 = J_x \sum_j S_j^x S_{j+1}^x, \end{aligned} \quad (3)$$

with N sites and periodic boundary conditions. The normalized classical spin variable \mathbf{S}_j on site j can also

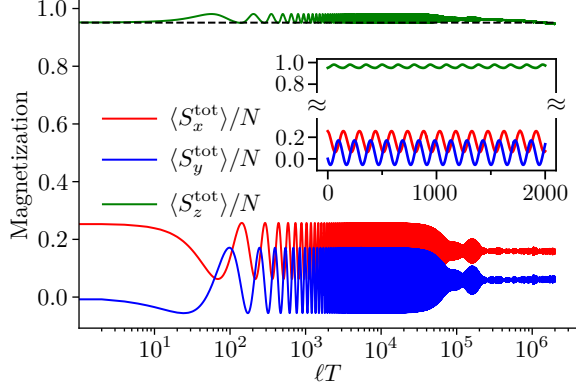


FIG. 1. Dynamics of the total magnetizations in a 1D driven Heisenberg-type model. Magnetization in the (x, y) -plane (red and blue) rotates periodically, suggesting the existence of mNGs. $\langle S_z^{\text{tot}} \rangle / N$ (green) oscillates on top of the conserved value (dashed line) due to higher order effects that break $O(2)$ symmetry. We use parameters $T=2$, $J_2=1$, $h_x=2$, $h_y=-2$, $J_x=2$, $\theta_j=0.2\pi$, and ϕ_j randomly sampled within $(-\pi/3, \pi/3)$.

be parametrized by azimuthal angle ϕ_j and polar angle θ_j as $S_j^x = \sin \theta_j \cos \phi_j$, $S_j^y = \sin \theta_j \sin \phi_j$, $S_j^z = \cos \theta_j$; it satisfies the Poisson bracket $\{S_i^\mu, S_j^\nu\} = \delta_{ij} \epsilon^{\mu\nu\rho} S_j^\rho$ with the fully antisymmetric tensor $\epsilon^{\mu\nu\rho}$. Here H_2 corresponds to the Heisenberg model, and H_1, H'_1 are generators of $O(3)$ symmetries; $h_{x/y}$ are the magnetic field strength along the x/y -directions, and J_x denotes the interaction strength along x -direction which breaks all continuous symmetries. The spin dynamics is described by $\dot{S}_j^\mu = \{S_j^\mu, H(t)\}$, where the time-dependence in the Hamiltonian follows the piecewise protocol, Eq. (1). Following Eq. (2) we obtain the effective Hamiltonian

$$Q_{\text{eff}} = -\frac{J_2}{5} \sum_j \mathbf{S}_j \cdot \mathbf{S}_{j+1} + \frac{h_x h_y T}{200} \sum_j S_j^z, \quad (4)$$

up to order $\mathcal{O}(T)$. $Q^{(0)}$ is the Heisenberg model preserving $O(3)$ and $Q^{(1)}$ degrades the symmetry to $O(2)$ around the z -axis. For $J_2 > 0$, the ground state features FM order (Case 1) along the positive (negative) z -direction if we take h_x and h_y of the opposite (same) sign [78].

In the high-frequency regime, the early-time spin dynamics approximately follows the EOM generated by Q_{eff} . If h_x and h_y have the opposite sign and considering the regime $S_j^z \approx 1$ and $S_j^{x/y} \ll 1$, one obtains the spin-wave spectrum via a standard linearization method

$$\omega = \pm \left[\frac{2J_2}{5} (1 - \cos q) + \frac{|h_x h_y| T}{200} \right], \quad (5)$$

with q denoting the quasi-momentum, cf. SM for details.

Similar to the Heisenberg model, a quadratic dispersion appears for long-wavelength modes ($q \rightarrow 0$). Yet, at $q=0$ this mode has a gap of size $|h_x h_y T|/200$ that is linear in T , matching our generic expectation as elaborated

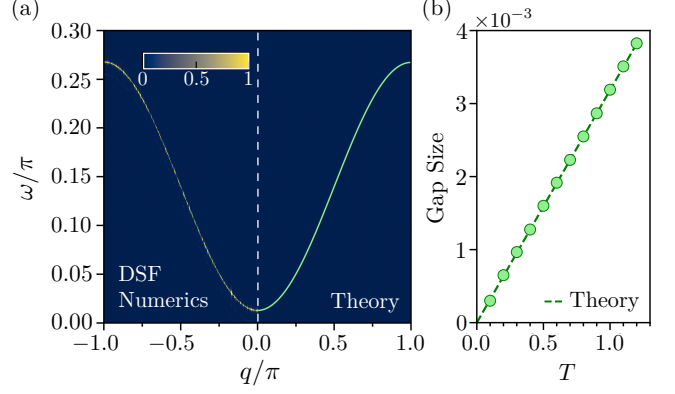


FIG. 2. (a) Dynamical structure factor (DSF) through the first Brillouin zone. The left half displays numerical results, which precisely follow the theoretical prediction (right half) and certify the existence of mNGs. We use the drive period $T=2$. The Fourier transform is performed by using 10^4 Floquet cycle. (b) A gap is opened at $q=0$ with a tunable size that depends linearly on T . We use $J_2=1$, $h_x=2$, $h_y=-2$, $J_x=1$, $\theta_j=0.01\pi$, and ϕ_j randomly sampled within $(-\pi/3, \pi/3)$.

above. The corresponding spin dynamics features a total magnetization in the (x, y) -plane rotating around the z -axis, with a frequency exactly matching the gap size. This dynamical behavior together with the dispersion relation thus provide a distinctive signature of the existence of mNGs that will be numerically verified below.

Numerical Results.— We now confirm the mNGs and discuss various hierarchical SB effects by investigating the Floquet spin dynamics. Initially, the system is prepared as an ensemble where spins deviate from the z -axis by a small angle θ_j , yielding a sufficiently large z -magnetization density, as required by the spin-wave approximation. The azimuthal angle ϕ_j is randomly sampled within a range s.t. the spatial randomness is sufficiently strong to generate many-body effects, but keeps a non-vanishing total magnetization in the (x, y) -plane.

For each driving step, the time evolution is governed by the EOM generated by the corresponding static Hamiltonian, except for H_2 where a symmetric Trotter decomposition is used for numerical efficiency [79]. For all numerical results we use $N=1000$ and perform ensemble averages over 100 realizations. The dynamics of the total magnetization components is shown in Fig. 1. The rotating magnetization in the (x, y) -plane (red and blue) is a characteristic signature of the mNGs. The oscillation is periodic in time (clearly visible in the inset where a linear time scale is used) and persists for a controllably long time without exhibiting any notable decay up to $\ell T \approx 10^5$. Although Q_{eff} in Eq. (4) conserves the z -magnetization and predicts a static $\langle S_z^{\text{tot}} \rangle / N$ (dashed line), the exact Floquet protocol indeed generates an oscillatory dynamics (green) since $Q^{(2)}$ breaks the $O(2)$ symmetry. Oscillations in the (x, y) -plane gradually damp out and settle into a prethermal plateau, which eventually heat up to an infinite temperature ensemble, cf. SM.

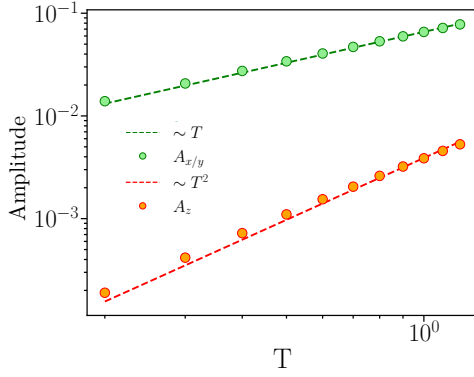


FIG. 3. Scaling of oscillation amplitudes, $A_{x/y} \propto T$ and $A_z \propto T^2$. It suggests that explicit symmetry breaking occurs hierarchically. The same parameters are used as in Fig. 2.

We further verify the entire mNG spectrum by analyzing the DSF $\mathcal{S}(q, \omega) = \langle |\mathbf{S}_q(\omega)|^2 \rangle$, where $\mathbf{S}_q(\omega)$ is the space-time Fourier transform of the spin configurations, $\mathbf{S}_q(\omega) = \sum_j \int dt \mathbf{S}_j(t) e^{-i(\omega t + qj)}$. Fig. 2(a) depicts $\mathcal{S}(q, \omega)$ for a fixed T : the spectrum precisely follows our theoretical prediction (green line in the right half), Eq. (5). A mNG gap opens at $q=0$ corresponding to the oscillatory frequency of the total magnetization. It is worth highlighting the controllability of the gap size by tuning the drive period, which also exhibits quantitative agreement with the theoretical prediction, as shown in Fig. 2(b).

$Q^{(2)}$ that cannot be captured by Eq. (4) breaks all symmetries, and hence modify and destabilize the mNGs. The most notable phenomenon is the oscillatory dynamics in $\langle S_z^{\text{tot}} \rangle / N$ as seen before in Fig. 1: it occurs because higher order corrections can effectively generate extra fields in the (x, y) -plane, slightly tilting the original explicit SB generator of the $O(2)$ symmetry in Q_{eff} . For low-temperature initial states and at short times, the three spin directions are indeed all coupled together by this field; therefore, they share the same oscillating frequency, cf. inset of Fig. 1. However, one clearly observes a difference in the oscillating amplitudes and $A_{x/y}$ is significantly larger than A_z . More precisely, in Fig. 3 we confirm their asymptotic scaling dependence on T , $A_{x/y} \sim T$ and $A_z \sim T^2$, which can also be analytically justified by a perturbative argument, cf. SM.

For even longer times, higher order effects together with thermal fluctuations (set by the spatial randomness in the initial states) lead to the damping of mNGs which broadens the spectrum. In Fig. 4 (a) we depict the Fourier spectrum for $q=0$. Strikingly, we observe an asymmetric lineshape and multiple side peaks of comparable heights, one intriguing non-equilibrium feature that normally does not exist in systems without driving. They depend on the details of the Trotterization protocol being used and also on the specific form of the SB processes, cf. SM.

The overall linewidth Γ in the DSF can be used to characterize the damping rate. It is determined by averaging

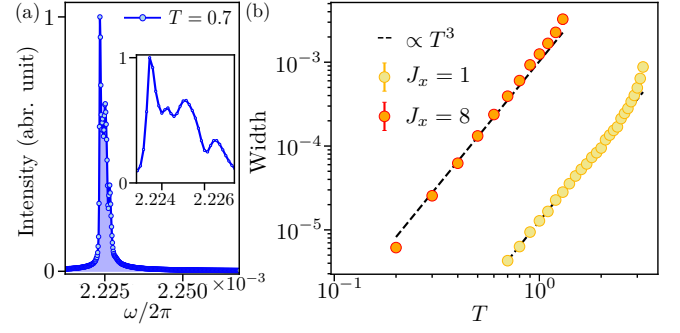


FIG. 4. (a) Fourier density for $J_x=1$. Damping of mNGs broadens the spectrum, leading to asymmetric lineshape and multiple side peaks that are shown in the inset. (b) Linewidth Γ exhibits a power-law scaling in the high frequency regime; the black dashed line with scaling T^3 is a guide to the eye. This scaling is different from the Fermi's Golden Rule expectation and can be justified by a hydrodynamic theory. We use $J_2=1$, $h_x=2$, $h_y=-2$, $\theta_j=0.25\pi$ and ϕ_j randomly sampled within $(-\pi/2, \pi/2)$.

the full width at 10%, 15%, and 20% of the maximum intensity of the Fourier peak, with their standard deviation serving as the error bar. Γ exhibits a power-law scaling T^α , suggesting that the mNGs lifetime can be systematically prolonged by increasing the drive frequency. Since all symmetries are broken by $\mathcal{O}(T^2)$ processes, following Fermi's Golden rule one may expect a scaling exponent $\alpha=4$ [80–82]; however, surprisingly, we find $\alpha \approx 3$, significantly deviating from this naive expectation.

We provide one possible explanation following a recent work [24], where the authors use hydrodynamics to analyse the damping rate of mNGs at the long wavelength limit. In the absence of explicit SB effects, for small q the magnons disperse as $\omega = \pm f q^2 - i \gamma q^4 + \dots$, where f determines the dispersion for the isotropic FM Heisenberg model; γ is generally non-zero at a finite temperature, originating from magnon-magnon scattering and thermal fluctuations [83–85]. When symmetries are weakly broken, this dispersion modifies to $\omega = \pm f(q_0^2 + q^2) - i(\Gamma + D_0 q^2 + \gamma q^4) + \dots$, with three additional parameters: the damping rate Γ , attenuation D_0 and the gap q_0^2 . Locality of constitutive relations in hydrodynamics implies that the damping rate for $q \rightarrow 0$ is completely determined by the relation $\Gamma = q_0^2(D_0 - \gamma q_0^2)$ [24].

Supposing the symmetry is broken only by a z -field as in Eq. (4), mNGs are stable for sufficiently low temperature, hence $D_0=0$. Therefore, contributions to D_0 should only involve $Q^{(2)}$ and higher-order perturbations. Together with the fact that the gap depends linearly on T , we know $q_0^2 \sim \mathcal{O}(T)$ and arrive at $\Gamma \sim \gamma \mathcal{O}(T^2) + \mathcal{O}(T^3)$. In all numerical simulations performed here, we consider initial states with a large z -magnetization density and small thermal fluctuations, hence γ can be extremely small. Therefore, the leading order in Γ can start from $\mathcal{O}(T^3)$. This indeed matches well with the numerical results in Fig. 4 (b), especially when the driving segment

H_0 that breaks the $O(2)$ symmetry is weak, $J_x=1$.

Discussion.— The scaling exponent of the mNGs lifetime may not be universal and can depend on Hamiltonian parameters. For instance, for the orange data shown in Fig. 4(b) with substantially stronger $O(2)$ SB effects, α is indeed larger than 3, see more examples in SM. To explain this scaling behavior one needs to further analyse the scattering channels between mNGs modes, e.g. the two- or three-magnon scattering matrix. Given different SB processes and thermal fluctuations, the dominant effects in D_0 may scale differently with T , and will be systematically studied in future work. As the scattering matrix now becomes tunable via Floquet-engineering, our work paves a new pathway to stabilize or create novel magnon bound states [58, 61, 86–88], as well as different transport behaviors which may not exist in non-driven systems.

While we have discussed the emergent mNGs in a classical Floquet system, we emphasize that our Floquet protocol applies equally to both quantum and classical systems. In SM, we present numerical simulations of a quantum system and certify the existence of mNGs [89], illustrating the possibility for experimentally detecting the mNGs in real quantum simulators.

Going beyond the present systems, it is intriguing to apply our general construction to physical systems exhibiting different types of mNGs. For instance, one can consider the Heisenberg model with anti-ferromagnetic couplings: a weak external z -field leads to a ground state manifold which preserves a $O(2)$ symmetry but this degeneracy is then lifted by $Q^{(2)}$ in driven systems (Case 2). As illustrated in SM, one mNG can still be detected from the spin dynamics. However, we observe strong evidence that the damping effect is substantially different

from the FM case, opening up new future directions [90].

Furthermore, the requirement that $Q^{(1)}$ forms a superposition of generators of the non-Abelian group G_2 , is not necessary for the appearance of mNGs, so long as $Q^{(1)}$ still preserves a subsymmetry of G_2 . We give one explicit example in the SM where $Q^{(1)}$ involves three-body interactions, which effectively generates a z -field for sufficiently small thermal fluctuations in the initial state. Yet, unlike the model in Eq. (4) where the gap size can be exactly determined, here the gap can only be computed approximately. Also, this mode tends to be very fragile with a notable broadening of the spectrum linewidth that scales linearly in T , see details in SM.

Generalizing the discussion to systems with long-range interactions [32] and higher-form symmetries [91–96], where anomalous or fractonic NGs may exist, also remains interesting to explore. Finally, beyond the Floquet paradigm, we envision the occurrence of mNGs in quasi-periodically [46, 97–99] and randomly driven systems [100].

Acknowledgments.— This work is supported by “The Fundamental Research Funds for the Central Universities, Peking University”, and by “High-performance Computing Platform of Peking University” and by the Deutsche Forschungsgemeinschaft under the cluster of excellence ct.qmat (EXC 2147, project-id 390858490). This work is funded by the European Union (ERC, QuSimCtrl, 101113633). Views and opinions expressed are however those of the authors only and do not necessarily reflect those of the European Union or the European Research Council Executive Agency. Neither the European Union nor the granting authority can be held responsible for them.

-
- [1] J. Goldstone, A. Salam, and S. Weinberg, Broken symmetries, *Physical Review* **127**, 965 (1962).
 - [2] H. Watanabe, Counting rules of nambu-goldstone modes, *Annual Review of Condensed Matter Physics* **11**, 169 (2020).
 - [3] Y. Nambu and G. Jona-Lasinio, Dynamical model of elementary particles based on an analogy with superconductivity. i, *Physical review* **122**, 345 (1961).
 - [4] S. Weinberg, Approximate symmetries and pseudo-goldstone bosons, *Physical review letters* **29**, 1698 (1972).
 - [5] S. Weinberg, *The quantum theory of fields*, Vol. 2 (Cambridge university press, 1995).
 - [6] S. Uchino, M. Kobayashi, M. Nitta, and M. Ueda, Quasi-nambu-goldstone modes in bose-einstein condensates, *Physical review letters* **105**, 230406 (2010).
 - [7] H. Watanabe and T. Brauner, Number of nambu-goldstone bosons and its relation to charge densities, *Physical Review D—Particles, Fields, Gravitation, and Cosmology* **84**, 125013 (2011).
 - [8] A. Kapustin, Remarks on nonrelativistic goldstone bosons, *arXiv preprint arXiv:1207.0457* (2012).
 - [9] H. Watanabe, T. Brauner, and H. Murayama, Massive nambu-goldstone bosons, *Physical Review Letters* **111**, 021601 (2013).
 - [10] A. Ncolis, R. Penco, F. Piazza, and R. A. Rosen, More on gapped goldstones at finite density: More gapped goldstones, *Journal of High Energy Physics* **2013**, 1 (2013).
 - [11] A. Ncolis and F. Piazza, Implications of relativity on nonrelativistic goldstone theorems: Gapped excitations at finite charge density, *Phys. Rev. Lett.* **110**, 011602 (2013).
 - [12] G. E. Marti, A. MacRae, R. Olf, S. Lourette, F. Fang, and D. M. Stamper-Kurn, Coherent magnon optics in a ferromagnetic spinor bose-einstein condensate, *Phys. Rev. Lett.* **113**, 155302 (2014).
 - [13] L. Liu, K. Chen, Y. Deng, M. Endres, L. Pollet, and N. Prokof'ev, Massive goldstone (higgs) mode in two-dimensional ultracold atomic lattice systems, *Physical Review B* **92**, 174521 (2015).
 - [14] M. A. Metlitski and T. Grover, Entanglement entropy of systems with spontaneously broken continuous symmetry, *arXiv preprint arXiv:1112.5166* (2011).

- [15] T. Hayata and Y. Hidaka, Dispersion relations of nambu-goldstone modes at finite temperature and density, *Physical Review D* **91**, 056006 (2015).
- [16] D. J. Luitz, X. Plat, F. Alet, and N. Laflorencie, Universal logarithmic corrections to entanglement entropies in two dimensions with spontaneously broken continuous symmetries, *Physical Review B* **91**, 155145 (2015).
- [17] B. Kulchytskyy, C. Herdman, S. Inglis, and R. G. Melko, Detecting goldstone modes with entanglement entropy, *Physical Review B* **92**, 115146 (2015).
- [18] K. Ohashi, T. Fujimori, and M. Nitta, Conformal symmetry of trapped bose-einstein condensates and massive nambu-goldstone modes, *Physical Review A* **96**, 051601 (2017).
- [19] J. Léonard, A. Morales, P. Zupancic, T. Donner, and T. Esslinger, Monitoring and manipulating higgs and goldstone modes in a supersolid quantum gas, *Science* **358**, 1415 (2017).
- [20] M. Guo, F. Böttcher, J. Hertkorn, J.-N. Schmidt, M. Wenzel, H. P. Büchler, T. Langen, and T. Pfau, The low-energy goldstone mode in a trapped dipolar supersolid, *Nature* **574**, 386 (2019).
- [21] A. Beekman, L. Rademaker, and J. Van Wezel, An introduction to spontaneous symmetry breaking, *SciPost Physics Lecture Notes*, 011 (2019).
- [22] K. T. Geier, G. I. Martone, P. Hauke, and S. Stringari, Exciting the goldstone modes of a supersolid spin-orbit-coupled bose gas, *Physical Review Letters* **127**, 115301 (2021).
- [23] H. Alaeian, G. Giedke, I. Carusotto, R. Löw, and T. Pfau, Limit cycle phase and goldstone mode in driven dissipative systems, *Physical Review A* **103**, 013712 (2021).
- [24] L. V. Delacrétaz, B. Goutéraux, and V. Ziegler, Damping of pseudo-goldstone fields, *Physical Review Letters* **128**, 141601 (2022).
- [25] Q.-Q. Shi, H.-Q. Zhou, I. P. McCulloch, and M. T. Batchelor, Type-b goldstone modes and a logarithmic spiral in the staggered su (4) ferromagnetic spin-orbital model, *arXiv preprint arXiv:2309.04973* (2023).
- [26] O. K. Diessel, S. Diehl, N. Defenu, A. Rosch, and A. Chiocchetta, Generalized higgs mechanism in long-range-interacting quantum systems, *Physical Review Research* **5**, 033038 (2023).
- [27] S. Khatua, M. J. Gingras, and J. G. Rau, Pseudo-goldstone modes and dynamical gap generation from order by thermal disorder, *Physical Review Letters* **130**, 266702 (2023).
- [28] J. Armas, A. Jain, and R. Lier, Approximate symmetries, pseudo-goldstones, and the second law of thermodynamics, *Physical Review D* **108**, 086011 (2023).
- [29] Y. Zhang, Y. Chen, H. Lyu, and Y. Zhang, Quantum phases in spin-orbit-coupled floquet spinor bose gases, *Physical Review Research* **5**, 023160 (2023).
- [30] T. Roscilde, T. Comparin, and F. Mezzacapo, Rotor/spin-wave theory for quantum spin models with u (1) symmetry, *Physical Review B* **108**, 155130 (2023).
- [31] M. Di Liberto and N. Goldman, Chiral orbital order of interacting bosons without higher bands, *Physical Review Research* **5**, 023064 (2023).
- [32] M. Song, J. Zhao, C. Zhou, and Z. Y. Meng, Dynamical properties of quantum many-body systems with long-range interactions, *Physical Review Research* **5**, 033046 (2023).
- [33] E. I. Kiselev, M. S. Rudner, and N. H. Lindner, Inducing plasmonic exceptional points and pattern formation with modulated floquet parametric driving, *arXiv preprint arXiv:2303.02148* (2023).
- [34] F. M. Surace and O. Motrunich, Weak integrability breaking perturbations of integrable models, *Phys. Rev. Res.* **5**, 043019 (2023).
- [35] J. R. M. de Nova and F. Sols, Simultaneous symmetry breaking in spontaneous floquet states: Floquet-nambu-goldstone modes, floquet thermodynamics, and the time operator, *arXiv preprint arXiv:2402.10784* (2024).
- [36] J. Ren, Y.-P. Wang, and C. Fang, Quasi-nambu-goldstone modes in many-body scar models, *arXiv preprint arXiv:2405.00785* (2024).
- [37] T. Kitagawa, E. Berg, M. Rudner, and E. Demler, Topological characterization of periodically driven quantum systems, *Physical Review B* **82**, 235114 (2010).
- [38] E. A. Martinez, C. A. Muschik, P. Schindler, D. Nigg, A. Erhard, M. Heyl, P. Hauke, M. Dalmonte, T. Monz, P. Zoller, et al., Real-time dynamics of lattice gauge theories with a few-qubit quantum computer, *Nature* **534**, 516 (2016).
- [39] A. C. Potter, T. Morimoto, and A. Vishwanath, Classification of interacting topological floquet phases in one dimension, *Physical Review X* **6**, 041001 (2016).
- [40] P. Titum, E. Berg, M. S. Rudner, G. Refael, and N. H. Lindner, Anomalous floquet-anderson insulator as a nonadiabatic quantized charge pump, *Physical Review X* **6**, 021013 (2016).
- [41] V. Khemani, A. Lazarides, R. Moessner, and S. L. Sondhi, Phase structure of driven quantum systems, *Physical review letters* **116**, 250401 (2016).
- [42] D. V. Else, B. Bauer, and C. Nayak, Floquet time crystals, *Physical review letters* **117**, 090402 (2016).
- [43] N. Y. Yao, A. C. Potter, I.-D. Potirniche, and A. Vishwanath, Discrete time crystals: Rigidity, criticality, and realizations, *Physical review letters* **118**, 030401 (2017).
- [44] T. Oka and S. Kitamura, Floquet engineering of quantum materials, *Annual Review of Condensed Matter Physics* **10**, 387 (2019).
- [45] C. Schweizer, F. Grusdt, M. Berngruber, L. Barbiero, E. Demler, N. Goldman, I. Bloch, and M. Aidelsburger, Floquet approach to z2 lattice gauge theories with ultracold atoms in optical lattices, *Nature Physics* **15**, 1168 (2019).
- [46] D. V. Else, W. W. Ho, and P. T. Dumitrescu, Long-lived interacting phases of matter protected by multiple time-translation symmetries in quasiperiodically driven systems, *Physical Review X* **10**, 021032 (2020).
- [47] H. Zhao, F. Mintert, R. Moessner, and J. Knolle, Random multipolar driving: Tunably slow heating through spectral engineering, *Physical Review Letters* **126**, 040601 (2021).
- [48] T. Mori, H. Zhao, F. Mintert, J. Knolle, and R. Moessner, Rigorous bounds on the heating rate in thue-morse quasiperiodically and randomly driven quantum many-body systems, *Phys. Rev. Lett.* **127**, 050602 (2021).
- [49] S. Geier, N. Thaicharoen, C. Hainaut, T. Franz, A. Salzinger, A. Tebben, D. Grimshandl, G. Zürn, and M. Weidemüller, Floquet hamiltonian engineering of an isolated many-body spin system, *Science* **374**, 1149 (2021).
- [50] P. T. Dumitrescu, J. G. Bohnet, J. P. Gaebler, A. Hankin, D. Hayes, A. Kumar, B. Neyenhuis, R. Vasseur,

- and A. C. Potter, Dynamical topological phase realized in a trapped-ion quantum simulator, *Nature* **607**, 463 (2022).
- [51] F. Petiziol, S. Wimberger, A. Eckardt, and F. Mintert, Non-perturbative floquet engineering of the toric-code hamiltonian and its ground state, *arXiv preprint arXiv:2211.09724* (2022).
- [52] X. Zhang, W. Jiang, J. Deng, K. Wang, J. Chen, P. Zhang, W. Ren, H. Dong, S. Xu, Y. Gao, et al., Digital quantum simulation of floquet symmetry-protected topological phases, *Nature* **607**, 468 (2022).
- [53] M. Kalinowski, N. Maskara, and M. D. Lukin, Non-abelian floquet spin liquids in a digital rydberg simulator, *Physical Review X* **13**, 031008 (2023).
- [54] H.-K. Jin, J. Knolle, and M. Knap, Fractionalized prethermalization in a driven quantum spin liquid, *Physical Review Letters* **130**, 226701 (2023).
- [55] B.-Y. Sun, N. Goldman, M. Aidelsburger, and M. Bukov, Engineering and probing non-abelian chiral spin liquids using periodically driven ultracold atoms, *PRX Quantum* **4**, 020329 (2023).
- [56] Z. Fu, R. Moessner, H. Zhao, and M. Bukov, *Engineering hierarchical symmetries* (2024), *arXiv:2402.13519 [quant-ph]*.
- [57] H.-K. Jin and J. Knolle, Floquet prethermal order by disorder, *arXiv preprint arXiv:2403.17118* (2024).
- [58] T. Fukuhara, P. Schauß, M. Endres, S. Hild, M. Cheneau, I. Bloch, and C. Gross, Microscopic observation of magnon bound states and their dynamics, *Nature* **502**, 76 (2013).
- [59] H. Sun, B. Yang, H.-Y. Wang, Z.-Y. Zhou, G.-X. Su, H.-N. Dai, Z.-S. Yuan, and J.-W. Pan, Realization of a bosonic antiferromagnet, *Nature Physics* **17**, 990 (2021).
- [60] X. Mi, M. Ippoliti, C. Quintana, A. Greene, Z. Chen, J. Gross, F. Arute, K. Arya, J. Atalaya, R. Babbush, et al., Time-crystalline eigenstate order on a quantum processor, *Nature* **601**, 531 (2022).
- [61] F. Kranzl, S. Birnkammer, M. K. Joshi, A. Bastianello, R. Blatt, M. Knap, and C. F. Roos, Observation of magnon bound states in the long-range, anisotropic heisenberg model, *Physical Review X* **13**, 031017 (2023).
- [62] M. Bukov, S. Gopalakrishnan, M. Knap, and E. Demler, Prethermal floquet steady states and instabilities in the periodically driven, weakly interacting bose-hubbard model, *Physical review letters* **115**, 205301 (2015).
- [63] T. Mori, T. Kuwahara, and K. Saito, Rigorous bound on energy absorption and generic relaxation in periodically driven quantum systems, *Physical review letters* **116**, 120401 (2016).
- [64] D. A. Abanin, W. De Roeck, and F. Huveneers, Exponentially slow heating in periodically driven many-body systems, *Physical review letters* **115**, 256803 (2015).
- [65] The coefficients c_{ijk} should contain non-vanishing elements otherwise the symmetry becomes Abelian. If so, the gap can only be generated by $Q^{(2)}$, which indeed also contains processes that destabilize mNGs; as a result, one cannot separately tune the gap and stability as in the non-Abelian case.
- [66] H. Watanabe, T. c. v. Brauner, and H. Murayama, Massive nambu-goldstone bosons, *Phys. Rev. Lett.* **111**, 021601 (2013).
- [67] In general, the new ground state will explicitly depend on T and the concrete form of $Q^{(2)}$, which contains complicated nested commutators of each Hamiltonian in the drive, making the analytical prediction of the mNGs very difficult in practice. We also note that, the inverse-frequency expansion for Floquet systems does not converge in general. However, as a dynamic consequence of this divergence, Floquet heating can be delayed up to exponentially long times. We emphasize that this is irrelevant to the Goldstone physics discussed here, which only persists for algebraically long times.
- [68] H. Zhao, M. Bukov, M. Heyl, and R. Moessner, Making trotterization adaptive and energy-self-correcting for nisq devices and beyond, *PRX Quantum* **4**, 030319 (2023).
- [69] K. Xu, J.-J. Chen, Y. Zeng, Y.-R. Zhang, C. Song, W. Liu, Q. Guo, P. Zhang, D. Xu, H. Deng, et al., Emulating many-body localization with a superconducting quantum processor, *Physical review letters* **120**, 050507 (2018).
- [70] S.-A. Guo, Y.-K. Wu, J. Ye, L. Zhang, W.-Q. Lian, R. Yao, Y. Wang, R.-Y. Yan, Y.-J. Yi, Y.-L. Xu, et al., A site-resolved two-dimensional quantum simulator with hundreds of trapped ions, *Nature*, 1 (2024).
- [71] C. Braun, R. Saint-Jalm, A. Hesse, J. Arceri, I. Bloch, and M. Aidelsburger, Real-space detection and manipulation of topological edge modes with ultracold atoms, *Nature Physics*, 1 (2024).
- [72] T. Mori, Floquet prethermalization in periodically driven classical spin systems, *Physical Review B* **98**, 104303 (2018).
- [73] O. Howell, P. Weinberg, D. Sels, A. Polkovnikov, and M. Bukov, Asymptotic prethermalization in periodically driven classical spin chains, *Physical review letters* **122**, 010602 (2019).
- [74] B. Ye, F. Machado, and N. Y. Yao, Floquet phases of matter via classical prethermalization, *Physical Review Letters* **127**, 140603 (2021).
- [75] A. Pizzi, A. Nunnenkamp, and J. Knolle, Classical prethermal phases of matter, *Physical Review Letters* **127**, 140602 (2021).
- [76] H.-K. Jin, A. Pizzi, and J. Knolle, Prethermal nematic order and staircase heating in a driven frustrated ising magnet with dipolar interactions, *Physical Review B* **106**, 144312 (2022).
- [77] A. J. McRoberts, H. Zhao, R. Moessner, and M. Bukov, Prethermalization in periodically driven nonreciprocal many-body spin systems, *Physical Review Research* **5**, 043008 (2023).
- [78] Note, Mermin-Wagner theorem does not apply here as the $O(3)$ symmetry is explicitly broken by a z -field, which can lead to finite magnetization even at a finite temperature.
- [79] Except for those generated by H_2 , the EOMs can be explicitly integrated over the corresponding step duration. For H_2 , we use a symmetric Trotter decomposition to approximate the evolution [77], thereby significantly improving the efficiency of the numerical simulations, cf. details in SM. This method introduces simulation errors at order $\mathcal{O}(T^2)$, and hence it neither changes the form of Q_{eff} , Eq. (4), nor gap size predicted above.
- [80] T. N. Ikeda and A. Polkovnikov, Fermi's golden rule for heating in strongly driven floquet systems, *Physical Review B* **104**, 134308 (2021).
- [81] N. O'Dea, F. Burnell, A. Chandran, and V. Khemani, Prethermal stability of eigenstates under high frequency

- floquet driving, *Phys. Rev. Lett.* **132**, 100401 (2024).
- [82] T. Mori, Heating rates under fast periodic driving beyond linear response, *Physical Review Letters* **128**, 050604 (2022).
 - [83] R. Tahir-Kheli and D. Ter Haar, Use of green functions in the theory of ferromagnetism. ii. dyson spin waves, *Physical Review* **127**, 95 (1962).
 - [84] A. B. Harris, Energy width of spin waves in the heisenberg ferromagnet, *Physical Review* **175**, 674 (1968).
 - [85] B. Halperin and P. Hohenberg, Hydrodynamic theory of spin waves, *Physical Review* **188**, 898 (1969).
 - [86] T. Macrì, L. Lepori, G. Pagano, M. Lewenstein, and L. Barbiero, Bound state dynamics in the long-range spin-1 xxz model, *Physical Review B* **104**, 214309 (2021).
 - [87] C. J. Turner, M. Szyniszewski, B. Mukherjee, R. Mendl, H. J. Changlani, and A. Pal, Stable infinite-temperature eigenstates in $su(2)$ -symmetric nonintegrable models, *arXiv preprint arXiv:2407.11956* (2024).
 - [88] K. Kim, F. Yang, K. Mølmer, and J. Ahn, Realization of an extremely anisotropic heisenberg magnet in rydberg atom arrays, *Phys. Rev. X* **14**, 011025 (2024).
 - [89] P. Weinberg and M. Bukov, QuSpin: a Python package for dynamics and exact diagonalisation of quantum many body systems part I: spin chains, *SciPost Phys.* **2**, 003 (2017).
 - [90] Indeed, $Q^{(0)} + Q^{(1)}$ also predicts a gapless mode with linear dispersion. However, it is unstable against higher order perturbations and we do not observe them in the exact Floquet dynamics.
 - [91] P. Sala, T. Rakovszky, R. Verresen, M. Knap, and F. Pollmann, Ergodicity breaking arising from hilbert space fragmentation in dipole-conserving hamiltonians, *Physical Review X* **10**, 011047 (2020).
 - [92] J.-K. Yuan, S. A. Chen, and P. Ye, Fractonic superfluids, *Physical Review Research* **2**, 023267 (2020).
 - [93] Y. Hidaka, Y. Hirono, and R. Yokokura, Counting nambu-goldstone modes of higher-form global symmetries, *Physical review letters* **126**, 071601 (2021).
 - [94] J. Armas and A. Jain, Approximate higher-form symmetries, topological defects, and dynamical phase transitions, *Physical Review D* **109**, 045019 (2024).
 - [95] A. Gromov and L. Radzihovsky, Colloquium: Fracton matter, *Reviews of Modern Physics* **96**, 011001 (2024).
 - [96] J. Boesl, P. Zechmann, J. Feldmeier, and M. Knap, Deconfinement dynamics of fractons in tilted bose-hubbard chains, *Physical Review Letters* **132**, 143401 (2024).
 - [97] P. T. Dumitrescu, R. Vasseur, and A. C. Potter, Logarithmically slow relaxation in quasiperiodically driven random spin chains, *Phys. Rev. Lett.* **120**, 070602 (2018).
 - [98] H. Zhao, F. Mintert, and J. Knolle, Floquet time spirals and stable discrete-time quasicrystals in quasiperiodically driven quantum many-body systems, *Physical Review B* **100**, 134302 (2019).
 - [99] D. M. Long and D. V. Else, *Topological phases of many-body localized systems: Beyond eigenstate order* (2024), *arXiv:2408.00825 [cond-mat.str-el]*.
 - [100] L. J. I. Moon, P. M. Schindler, Y. Sun, E. Druga, J. Knolle, R. Moessner, H. Zhao, M. Bukov, and A. Ajoy, *Experimental observation of a time rondeau crystal: Temporal disorder in spatiotemporal order* (2024), *arXiv:2404.05620 [quant-ph]*.

Supplementary Material
Floquet-engineered Emergent Massive Nambu-Goldstone Modes

CONTENTS

SM 1. Continuous Driving Protocol	9
SM 2. Further Analysis for Ferromagnetic Systems	10
1. Derivation for the Spin-wave Spectrum, Eq. (5)	10
2. Oscillating Amplitudes of Quasi-conserved Quantities in Classical Spin Systems	10
3. Asymmetric Lineshape and Side Peaks	11
4. Different Scaling of Linewidth	12
5. Thermalization and Hierarchical Symmetry Breaking in Prethermal Plateaus	13
6. Classical System with Three-body Interactions	13
7. Ferromagnetic Quantum Spin Model	16
SM 3. Massive Nambu-Goldstone Modes in Floquet Anti-ferromagnetic Systems	18
1. Spin-wave Theory	18
2. Numerical Verification of Massive Goldstone Modes	19
SM 4. Trotterized Simulation Protocol	20

SM 1. CONTINUOUS DRIVING PROTOCOL

The protocol proposed in the main text involves discrete drives that can be implemented on digital quantum simulators. For analog platforms, like cold atoms, a continuous driving protocol is preferred. Here, we present one possible continuous protocol that can achieve a similar effective Hamiltonian to generate mNGs.

Consider a unitary time evolution operator

$$U_F = \mathcal{T} e^{-i \int_0^T H(t) dt} \equiv e^{-iTQ} \quad (\text{S.1})$$

where $H(t+T) = H(t)$ is a time-periodic Hamiltonian and Q is the effective Hamiltonian. Q can be obtained by the high-frequency expansion and its lowest two orders read

$$Q^{(0)} \propto K_0, \quad Q^{(1)} \propto T \sum_{l=1}^{\infty} \frac{1}{l} [K_l, K_{-l}], \quad (\text{S.2})$$

where K_l denotes the Fourier harmonics of $H(t)$, i.e., $H(t) = \sum_l K_l e^{il\omega t}$. Suppose the time-dependent Hamiltonian has the form

$$H(t) = K_0 + K_1 \cos \omega t + K'_1 \sin \omega t + K_2 \cos 2\omega t \quad (\text{S.3})$$

where K_0 preserves a symmetry group G_2 , K_1 and K'_1 are two non-commuting generators of G_2 , and K_2 further breaks all symmetries. Then the effective Hamiltonian reduces to $Q^{(0)} \propto K_0$, $Q^{(1)} \propto iT[K_1, K'_1]$ and higher-order terms break all symmetries. Hence, this protocol can effectively realize similar mNGs as in the main text but with continuous drives.

SM 2. FURTHER ANALYSIS FOR FERROMAGNETIC SYSTEMS

1. Derivation for the Spin-wave Spectrum, Eq. (5)

Based on Eq. (4) and $\dot{S}_j^\mu = \{S_j^\mu, Q_{\text{eff}}\}$, one can derive the EOM

$$\begin{aligned}\dot{S}_j^x &= \frac{J_2}{5} [(S_{j-1}^z + S_{j+1}^z) S_j^y - (S_{j-1}^y + S_{j+1}^y) S_j^z] - \frac{h_x h_y T}{200} S_j^y, \\ \dot{S}_j^y &= \frac{J_2}{5} [(S_{j-1}^x + S_{j+1}^x) S_j^z - (S_{j-1}^z + S_{j+1}^z) S_j^x] + \frac{h_x h_y T}{200} S_j^x, \\ \dot{S}_j^z &= \frac{J_2}{5} [(S_{j-1}^y + S_{j+1}^y) S_j^x - (S_{j-1}^x + S_{j+1}^x) S_j^y].\end{aligned}\tag{S.4}$$

To derive the mNGs spectrum, we employ a standard linearization method and consider the regime, $S_j^z \approx 1$ and $S_j^{x/y} \ll 1$, assuming that h_x and h_y have the opposite sign. Neglecting non-linear terms in $S_j^{x/y}$, we obtain

$$\begin{aligned}\dot{S}_j^x &= \frac{J_2}{5} (2S_j^y - S_{j-1}^y - S_{j+1}^y) - \frac{h_x h_y T}{200} S_j^y, \\ \dot{S}_j^y &= \frac{J_2}{5} (S_{j-1}^x + S_{j+1}^x - 2S_j^x) + \frac{h_x h_y T}{200} S_j^x, \\ \dot{S}_j^z &= 0.\end{aligned}\tag{S.5}$$

This can be solved analytically by performing a Fourier transform, $S_j^\alpha = \sum_q S_q^\alpha e^{i(qa)j}$, $\alpha \in \{x, y, z\}$, with q denoting the quasi-momentum and a being the lattice constant. Finally we get the spin-wave spectrum, Eq. (5)

$$\omega = \pm \left[\frac{2J_2}{5} (1 - \cos qa) + \frac{|h_x h_y| T}{200} \right].\tag{S.6}$$

In all numerical simulations, we take $a = 1$.

2. Oscillating Amplitudes of Quasi-conserved Quantities in Classical Spin Systems

The oscillatory dynamics of the z -component magnetization, shown in Fig. 1, cannot be explained by the truncated effective Hamiltonian, Eq. (4). In Fig. 3, we show that the oscillating amplitude of the total magnetization in different directions can have different dependence on the drive period T . Here we provide one perturbative argument to justify this behavior.

Drive-induced terms $Q^{(2)}$ of order $\mathcal{O}(T^2)$ break the $O(2)$ symmetry along the z -axis. Therefore, in the linearized regime where spins are mostly polarized in the z direction, $Q^{(2)}$ effectively generate weak fields in the (x, y) -plane. One can approximately describe this situation via the Hamiltonian

$$H = -J_2 \sum_j \mathbf{S}_j \cdot \mathbf{S}_{j+1} - h(h_x \sum_j S_j^x + h_y \sum_j S_j^y + h_z \sum_j S_j^z),\tag{S.7}$$

where $h_x^2 + h_y^2 + h_z^2 = 1$, and h quantifies the strength of the field. In the high frequency regime, we expect $h \sim T$, $h_{x/y} \sim T$ and $h_z \sim 1$ for small drive periods T . The ground state of this Hamiltonian is $\vec{S}_j = (h_x, h_y, h_z)$ for all sites. One can obtain the linearized EOM

$$\begin{aligned}\dot{S}_j^x &= J_2 [h_y (S_{j-1}^z + S_{j+1}^z - 2S_j^z) + h_z (-S_{j-1}^y - S_{j+1}^y + 2S_j^y) + h(-h_y S_j^z + h_z S_j^y)], \\ \dot{S}_j^y &= J_2 [h_z (S_{j-1}^x + S_{j+1}^x - 2S_j^x) + h_x (-S_{j-1}^z - S_{j+1}^z + 2S_j^z) + h(-h_z S_j^x + h_x S_j^z)], \\ \dot{S}_j^z &= J_2 [h_x (S_{j-1}^y + S_{j+1}^y - 2S_j^y) + h_y (-S_{j-1}^x - S_{j+1}^x + 2S_j^x) + h(-h_x S_j^y + h_y S_j^x)].\end{aligned}\tag{S.8}$$

By Fourier transforming $S_j^\alpha = \sum_q S_q^\alpha e^{i(qa)j}$ we have

$$\dot{\mathbf{S}}_q = [2J_2(1 - \cos qa) + h] \begin{pmatrix} 0 & h_z & -h_y \\ -h_z & 0 & h_x \\ h_y & -h_x & 0 \end{pmatrix} \mathbf{S}_q \equiv A_q \mathbf{S}_q.\tag{S.9}$$

The solution of the ODE reads

$$\mathbf{S}_q(t) = e^{A_q t} \mathbf{S}_q(0), \quad (\text{S.10})$$

with the expression

$$e^{A_q t} = \begin{pmatrix} (h_y^2 + h_z^2) \cos(\omega t) + h_x^2 & 2h_x h_y \sin^2(\frac{1}{2}\omega t) + h_z \sin(\omega t) & 2h_x h_z \sin^2(\frac{1}{2}\omega t) - h_y \sin(\omega t) \\ 2h_x h_y \sin^2(\frac{1}{2}\omega t) - h_z \sin(\omega t) & h_x^2 \cos(\omega t) + h_z^2 \cos(\omega t) + h_y^2 & 2h_y h_z \sin^2(\frac{1}{2}\omega t) + h_x \sin(\omega t) \\ 2h_x h_z \sin^2(\frac{1}{2}\omega t) + h_y \sin(\omega t) & 2h_y h_z \sin^2(\frac{1}{2}\omega t) - h_x \sin(\omega t) & h_x^2 \cos(\omega t) + h_y^2 \cos(\omega t) + h_z^2 \end{pmatrix}, \quad (\text{S.11})$$

suggesting an oscillatory dynamics with frequency $\omega = 2J_2(1 - \cos qa) + h$. It is important to notice that, although the field strength in the (x, y) -plane is much smaller than the z -field, the oscillations in three directions couple together and share the same frequency. However, the oscillating amplitudes are different, if the initial states are almost polarized in the z -direction, $S_q^{x/y} \ll 1$. More precisely, as long as $S_q^{x/y}$ is of order $\mathcal{O}(T)$ or even smaller, the third column of the matrix in Eq. (S.11) will dominate the dynamics, and the oscillating amplitudes scale as $A_{x/y} \sim T$ and $A_z \sim T^2$.

3. Asymmetric Lineshape and Side Peaks

The DSF has an asymmetric lineshape, as shown in Fig. 4(a). Also, several side peaks can be clearly resolved, one intriguing and rare non-equilibrium phenomenon in systems without external driving. We conjecture that the side peaks originate from $Q^{(3)}$ of order $\mathcal{O}(T^3)$, a high-order and weak process. Also, it can be slightly enhanced by Trotter decomposition being used to approximate the Heisenberg Hamiltonian evolution. To demonstrate this, we compare the numerical simulation generated by Q_{eff} and different order Trotter decomposition.

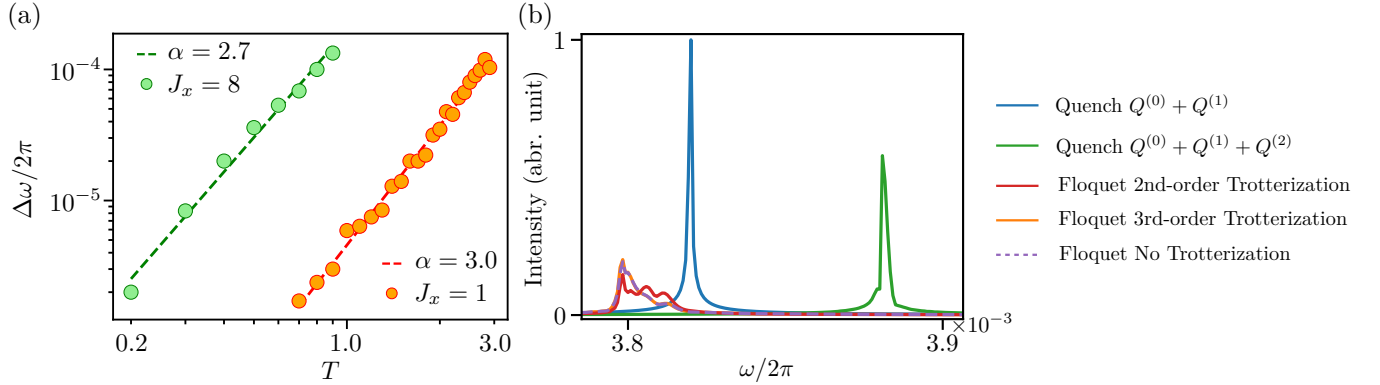


FIG. S1. (a) The splitting between the main peak and the highest side peak $\Delta\omega$ exhibits a power-law scaling as $\Delta\omega \sim T^\alpha$, $\alpha \approx 3$, suggesting that these peaks may be generated by $Q^{(3)}$ of order $\mathcal{O}(T^3)$. (b) Fourier peaks obtained by various numerical methods. We use $T=1.2$ and $J_x=1$. The lineshape becomes asymmetric once $Q^{(2)}$ is included. Fine structures in the lineshape appear in Floquet driven systems. 3rd-order Trotterization leads to Fourier spectrum that is almost identical to those obtained without the Trotterization. 2nd order Trotter slightly enhances the side peaks, although the overall linewidth remains approximately unchanged. We use $J_2=1$, $h_x=2$, $h_y=-2$, $\theta_j=0.25\pi$ and ϕ_j randomly sampled within $(-\pi/2, \pi/2)$. 100 ensemble averages are performed to the system with its size $N = 1000$.

We extract the splitting between the main peak and the highest side peak $\Delta\omega$ and plot it in Fig. S1(a) for different driving period. $\Delta\omega$ exhibits a power-law dependence on the driving period T with the exponent $\alpha \approx 3$.

We try to reproduce the interesting lineshape by several different numerical methods:

1. Quenching the initial states with static effective Hamiltonians, truncated at different orders $\mathcal{O}(T)$ and $\mathcal{O}(T^2)$.
2. Floquet driving the system and approximating the Heisenberg Hamiltonian H_2 using Trotter decomposition of different orders. Details of this method will be explained later in Sec. SM 4.
3. Floquet driving the system but evolving H_2 using a Runge-Kutta solver.

The results are shown in Fig. S1(b). For $Q^{(0)} + Q^{(1)}$, mNGs are exact low-energy quasi-particles and thermal fluctuation broadens the peak in a symmetric way (blue). The inclusion of $Q^{(2)}$ causes a peak shift and also the lineshape becomes asymmetric (green). For Floquet systems without Trotter decomposition (purple), the center of the Fourier peak shifts again and starts to exhibit interesting fine structures, e.g., shoulder on the right side of the main peak. Although not shown, for a smaller driving period side peaks also arise. Hence, one can conclude that $Q^{(2)}$,

that breaks all symmetries, is sufficient to generate asymmetric lineshape, but the fine structures, e.g. the splitting of the main peak, shoulders or side peaks, originate from $Q^{(3)}$ of order $\mathcal{O}(T^3)$. This also qualitatively explains the scaling exponent in the splitting observed in Fig. S1(a). The 3rd order Trotter approximation leads to almost identical results (orange). Interestingly, the 2nd order Trotter decomposition leads to more visible side peaks.

It is worth pointing out that, although the 2nd Trotterization being used in the main text results in a slightly different lineshape, compared the Runge-Kutta results, the overall linewidths are approximately the same, as shown in Fig. S2.

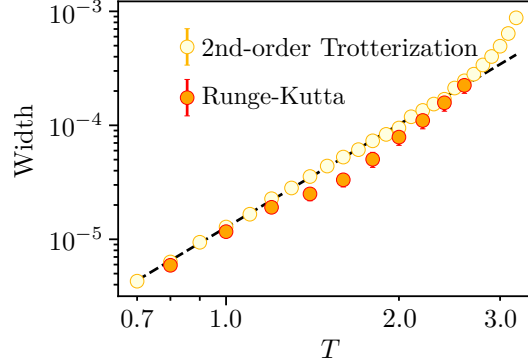


FIG. S2. The linewidth of the Fourier spectrum for different simulation methods. The Trotter protocol generates a slightly larger linewidth, but it closely mimics Runge-Kutta solver. We use $J_2=1$, $h_x=2$, $h_y=-2$, $J_x=1$ $\theta_j=0.25\pi$ and ϕ_j randomly sampled within $(-\pi/2, \pi/2)$. 100 ensemble averages are performed to the system with its size $N = 1000$.

4. Different Scaling of Linewidth

In the main text, Fig. 4, we find that the linewidth of DSF scales as T^3 , and we give one possible explanation using a hydrodynamic theory. One key assumption we made is that the attenuation D_0 , induced by explicit SB, is dominated by $Q^{(2)}$. Together with the scaling of the gap size, one estimates the damping rate as $\Gamma \sim T^3$.

However, this scaling may not be universal, and it can depend on the driving parameters and the randomness in the initial state ensemble.

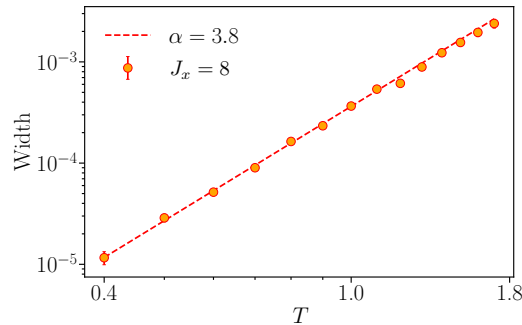


FIG. S3. The width Γ exhibits a power-law scaling in the high frequency regime; the dashed line with has fitted scaling $\alpha \approx 4$. We use $N=1000$, $J_2=1$, $h_x=2$, $h_y=-2$ for numerical simulations. Ensemble averaging over 100 realizations is performed with $\theta_j=0.1\pi$ and azimuthal angles ϕ_j randomly sampled within $(-\pi/3, \pi/3)$.

We perform further numerical simulations, using the same parameters as the orange dots in Fig. 4(b) but with an initial ensemble with a larger z -magnetization, corresponding to a lower temperature. Yet, as shown in Fig. S3, a scaling exponent $\alpha \approx 4$ appears. The reason could be that, although in the high frequency limit the dominant terms in D_0 scale as T^2 , its resulting physical effects may have a more complicated dependence on T . Identifying all possible mechanisms for the damping process, and understanding the relation between the hydrodynamics theory and Fermi's Golden rule in this setting, would require substantially more work, which goes beyond the scope of the current study.

5. Thermalization and Hierarchical Symmetry Breaking in Prethermal Plateaus

Floquet systems generally heat up to infinite temperature, due to the absence of energy conservation. However, this can take a long time, with a timescale that normally increases exponentially with the driving frequency [63, 64]. In Fig. 1 in the main text, to show the persistent periodic oscillation of the magnetization we use a small T , which indeed significantly delays the onset of heating. During the time window that we can numerically simulate, the system does not heat up to infinite temperature, but stays in a prethermal plateau. Here, instead, we use a smaller driving frequency and stronger symmetry breaking strength J_x to speed up heating. As shown in Fig. S4, after the initial transient oscillation, the system relaxes towards a prethermal plateau. Eventually, magnetization in three directions decays to zero, confirming the eventual heat death.

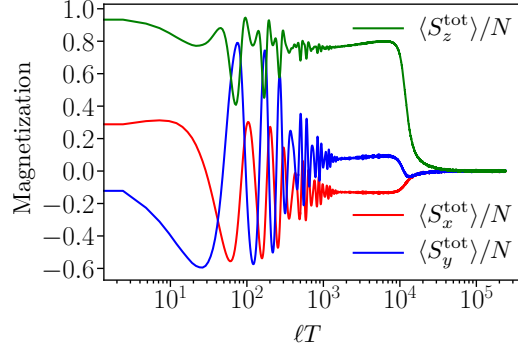


FIG. S4. Dynamics of the 1D driven Heisenberg-type model, Eq. (3), that shows the eventual thermalization. We use $N=1000$, $T=2.4$, $J_2=1$, $h_x=2$, $h_y=-2$, $J_x=5$ for numerical simulations. Ensemble averaging over 100 realizations is performed with $\theta_j=0.1\pi$ and azimuthal angles ϕ_j randomly sampled within $(-\pi/3, \pi/3)$.

Furthermore, Ref. [56] predicts a hierarchical symmetry-breaking effect in the prethermal plateau of quasi-conservation laws. To observe this phenomenon, initial states need to be sufficiently random, or high-temperature, but still keeping finite magnetization in the three directions. In the current setup, this effect is difficult to observe since the initial state is close to the ground state and the $Q^{(1)}$ term that breaks the $O(3)$ symmetry only generates a z -field, which can be gauged away by performing a rotating frame transformation. Therefore, the many-body system can not relax to a thermal ensemble corresponding to the truncated Hamiltonian $Q^{(0)} + Q^{(1)}$. To verify this phenomenon in classical spin systems, we use the following Floquet protocol

$$U_F = (e^{iH_0 \frac{T}{6}} e^{iH_1 \frac{T}{6}}) e^{-iH_2 \frac{T}{6}} (e^{-iH_0 \frac{T}{6}} e^{-iH_1 \frac{T}{6}}) e^{-iH_2 \frac{T}{6}}, \quad (\text{S.12})$$

with the Hamiltonians

$$H_2 = -J_2 \sum_j \mathbf{S}_j \cdot \mathbf{S}_{j+1}, \quad H_1 = -H_2 + J_1 \sum_{j \in \text{even}} S_j^z S_{j+2}^z, \quad H_0 = J_x \sum_{j \in \text{odd}} S_j^x S_{j+2}^x. \quad (\text{S.13})$$

Fig. S5 (a) shows the numerical time evolution of the total magnetization. From a sufficiently random initial ensemble, all components of the magnetization quickly settle into prethermal plateaus before eventually heating up to infinite temperature. A hierarchy in the prethermal lifetime is observed, and the z -component exhibits a more stable plateau that persists longer than those of the x and y components. Moreover, Ref. [56] predicts that the prethermal lifetime τ can be parametrically prolonged by using smaller driving period T , $\tau_{x/y} \sim T^{-2}$ and $\tau_z \sim T^{-4}$, following the Fermi Golden Rule argument. There, this scaling has been numerically verified in quantum systems of a small size. In Fig. S5 (b) we also observe this scaling law in our classical systems where finite-size effects are negligible.

6. Classical System with Three-body Interactions

To realize emergent mNGs, explicit SB processes in $Q^{(1)}$ are not limited to being a generator of the non-Abelian group G_2 , as long as $Q^{(1)}$ still preserves a subsymmetry of G_2 . Here, we present an explicit example that realizes the symmetry-breaking process, $O(3) - O(2) - E$, and $Q^{(1)}$ involves three-body interactions which is not a simple

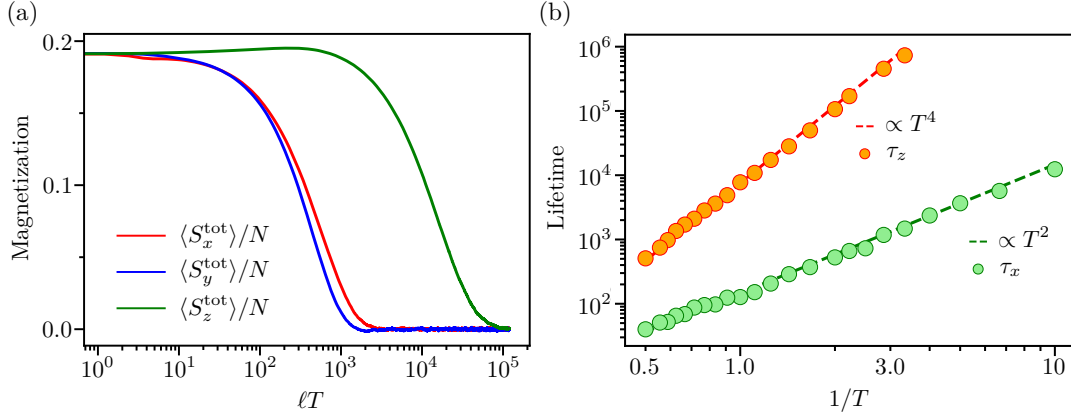


FIG. S5. (a) Dynamics of the Floquet system, Eq. (S.12). The prethermal plateaus for magnetization in z direction survives longer than the other two, showing a hierarchy in symmetry breaking phenomenon. (b) We define the lifetime τ as the time when the magnetizations drop below the threshold value 0.16. τ exhibits a power law dependence on the driving period, following the form $\tau \sim T^{-\alpha}$ where $\alpha \approx 2$ for the x (green dots) and y (not shown but nearly coinciding with the x -component) components, and $\alpha \approx 4$ for the z (orange dots) components. This scaling is consistent with the Fermi's Golden Rule expectation. We use $N=100$, $J_2=1$, $J_1=1$, $J_x=1$ for numerical simulations. Ensemble averaging over 800 realizations is performed with the initial state where 40% of the sites are prepared as $S_j^x = S_j^y = S_j^z = 1/\sqrt{3}$, while the remaining 60% are randomly sampled.

generator of the $O(3)$ group. We still observe emergent mNGs with controllable dispersion relation that can be tuned by T . However, those mNGs have a shorter lifetime that scales linearly with the driving frequency.

Consider a classical spin chain described by the protocol Eq. (1) with the Hamiltonians

$$\begin{aligned} H_2 &= -J_2 \sum_j \mathbf{S}_j \cdot \mathbf{S}_{j+1}, H_1 = J_1 \sum_j S_{j-1}^y S_j^y S_{j+1}^x + S_{j-1}^y S_j^x S_{j+1}^y - S_{j-1}^x S_j^z S_{j+1}^z, \\ H'_1 &= h_y \sum_j S_j^y - H_1, H_0 = J_x \sum_j S_j^x S_{j+1}^x. \end{aligned} \quad (\text{S.14})$$

We obtain the effective Hamiltonian up to order $\mathcal{O}(T)$

$$Q_{\text{eff}} = -\frac{J_2}{5} \sum_j \mathbf{S}_j \cdot \mathbf{S}_{j+1} + \frac{J_1 h_y T}{200} \sum_j (S_{j-1}^x S_j^x + S_{j-1}^y S_j^y) S_{j+1}^z - S_{j-1}^z S_j^z S_{j+1}^z + (S_{j-1}^x S_{j+1}^x + S_{j-1}^y S_{j+1}^y) S_j^z. \quad (\text{S.15})$$

$Q^{(0)}$ preserves $O(3)$ and $Q^{(1)}$ contains only the exchange terms and the z -component terms, therefore reducing the symmetry to $O(2)$ around the z -axis. We take $J_2 > 0$ such that the ground state features the FM order along the positive (negative) z -direction if J_1 and h_y have the same (opposite) sign. The EOM generated by the truncated Hamiltonian Eq. (S.15) read as

$$\begin{aligned} \dot{S}_j^x &= \frac{J_2}{5} [(S_{j-1}^z + S_{j+1}^z) S_j^y - (S_{j-1}^y + S_{j+1}^y) S_j^z] + \frac{J_1 h_y T}{200} [S_{j+1}^y S_j^z S_{j+2}^z + S_{j-1}^y S_j^z S_{j+1}^z + S_{j+2}^y S_j^z S_{j+1}^z + S_{j-2}^y S_j^z S_{j-1}^z \\ &\quad + S_j^y (S_{j+1}^z S_{j+2}^z + S_{j-1}^z S_{j+1}^z + S_{j-1}^z S_{j-2}^z) - (S_{j-1}^x S_{j-2}^x + S_{j-1}^y S_{j-2}^y + S_{j-1}^x S_{j+1}^x + S_{j-1}^y S_{j+1}^y) S_j^y], \\ \dot{S}_j^y &= \frac{J_2}{5} [(S_{j-1}^x + S_{j+1}^x) S_j^z - (S_{j-1}^z + S_{j+1}^z) S_j^x] - \frac{J_1 h_y T}{200} [S_{j+1}^x S_j^z S_{j+2}^z + S_{j-1}^x S_j^z S_{j+1}^z + S_{j+2}^x S_j^z S_{j+1}^z + S_{j-2}^x S_j^z S_{j-1}^z \\ &\quad + S_j^x (S_{j+1}^z S_{j+2}^z + S_{j-1}^z S_{j+1}^z + S_{j-1}^z S_{j-2}^z) - (S_{j-1}^x S_{j-2}^x + S_{j-1}^y S_{j-2}^y + S_{j-1}^x S_{j+1}^x + S_{j-1}^y S_{j+1}^y) S_j^y], \\ \dot{S}_j^z &= \frac{J_2}{5} [(S_{j-1}^y + S_{j+1}^y) S_j^x - (S_{j-1}^x + S_{j+1}^x) S_j^y] + \frac{J_1 h_y T}{200} [S_{j+2}^z (S_{j+1}^x S_j^y - S_{j+1}^y S_j^x) + S_{j+1}^z (S_{j-1}^x S_j^y - S_{j-1}^y S_j^x) \\ &\quad + S_{j+1}^z (S_{j+2}^x S_j^y - S_{j+2}^y S_j^x) + S_{j-1}^z (S_{j-2}^x S_j^y - S_{j-2}^y S_j^x)]. \end{aligned} \quad (\text{S.16})$$

We then proceed to show the existence of emergent mNGs by employing a standard linearization method. Similarly, we consider the regime where $S_j^z \approx 1$ and $S_j^{x/y} \ll 1$ (assuming J_1 and h_y have the opposite sign), and neglect non-linear

terms in $S_j^{x/y}$, obtaining the linearized EOM

$$\begin{aligned}\dot{S}_j^x &= \frac{J_2}{5}(2S_j^y - S_{j-1}^y - S_{j+1}^y) + \frac{J_1 h_y T}{200}(3S_j^y + S_{j-1}^y + S_{j+1}^y + S_{j-2}^y + S_{j+2}^y), \\ \dot{S}_j^y &= \frac{J_2}{5}(S_{j-1}^x + S_{j+1}^x - 2S_j^x) - \frac{J_1 h_y T}{200}(3S_j^x + S_{j-1}^x + S_{j+1}^x + S_{j-2}^x + S_{j+2}^x), \\ \dot{S}_j^z &= 0.\end{aligned}\tag{S.17}$$

Note that linearization effectively treats the three-body interactions as a field term that points in the z -direction. The spin-wave spectrum now reads

$$\omega = \pm \left[\frac{2J_2}{5}(1 - \cos qa) + \frac{J_1 h_y T}{200}(3 + 2 \cos qa + 2 \cos 2qa) \right], \tag{S.18}$$

A quadratic dispersion appears for modes of long wavelength when $q \rightarrow 0$ and a gap is now opened at $q = 0$ of size $|\frac{7J_1 h_y T}{200}|$ that is linear in T .

We now confirm the mNG modes and discuss their interplay with hierarchical explicit SB processes, by investigating the spin dynamics generated by the exact Floquet protocol. For the evolution generated by H_1 and H'_1 we numerically integrate the EOMs with the standard Runge-Kutta method. Aside from that, we use the same technique as the main text to numerically simulate the system.

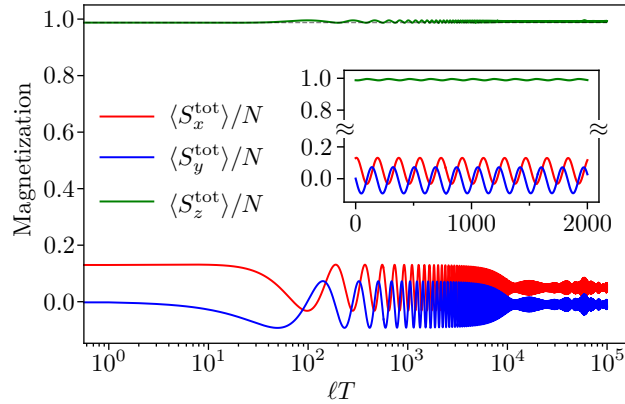


FIG. S6. Dynamics of the total magnetization in a 1D driven three-body interaction model, cf. Eq. (S.14). Magnetization in the (x, y) -plane (red and blue) rotates periodically, confirming the existence of mNGs. $\langle S_z^{\text{tot}} \rangle / N$ (green) oscillates on top of the conserved value (dashed line) due to higher order effects. We use a system of size $N = 1000$ and parameters $T=1$, $J_2=1$, $h_y=1$, $J_1=1$, $J_x=1$. We perform ensemble averages over 100 realizations where initial spins deviate from the z -axis by one small angle $\theta_j = 0.05\pi$, and their azimuthal angles ϕ_j are randomly sampled in the range $(-\pi/3, \pi/3)$.

The initial states are chosen such that $\theta_j = 0.025\pi$, and azimuthal angles ϕ_j randomly sampled within $(-\pi/3, \pi/3)$. Here θ_j is close to 0 and hence the condition $S_j^z \approx 1$ is well satisfied. The dynamics of the total magnetizations is shown in Fig. S6. The rotating magnetization in the (x, y) -plane (red and blue) suggests the appearance of the mNGs.

We further verify the entire mNG spectrum by analyzing the DSF $\mathcal{S}(q, \omega)$. Fig. S7(a) depicts $\mathcal{S}(q, \omega)$ for a fixed T , and the spectrum precisely follows our theoretical prediction, Eq. (S.18). A mNG gap opens at $q = 0$ and its size can also be tuned by the drive period, as shown in Fig. S7(b).

Similar behavior in the oscillating amplitudes ($A_{x/y} \sim T$, $A_z \sim T^2$) also appears here, see Fig. S8.

For even longer times, the damping of mNG modes broadens the spectrum and induces a finite linewidth Γ in DSF. We extract Γ for $q = 0$ by performing Fourier transform on the dynamics of the total magnetization components over time, and plot it in Fig. S9 for varying T . The linewidth is determined by averaging the full-width at 10%, 15%, and 20% of the maximum intensity of the Fourier peak, with their standard deviation serving as an error bar. Γ exhibits a power-law scaling T^α . However, in contrast to Fig. 4, here the scaling exponent is about 1, cf. Fig. S9, and hence mNGs are not very robust. Such a scaling implies that a $Q^{(1)}$ of order $\mathcal{O}(T)$ can destabilize mNGs, even if it preserves the $O(2)$ symmetry. The approximation that one can treat the three-body interaction as an effective $O(3)$ generator fails after a time scale that scales as $\mathcal{O}(T^{-1})$. Therefore, the damping of mNGs becomes notable shortly after the failure of linearization. We simulate the spin dynamics by using the truncated Hamiltonian, Eq. (S.15), and the results (green dots) are depicted in Fig. S9(a). In the high frequency regime, the linewidth for this quenched protocol

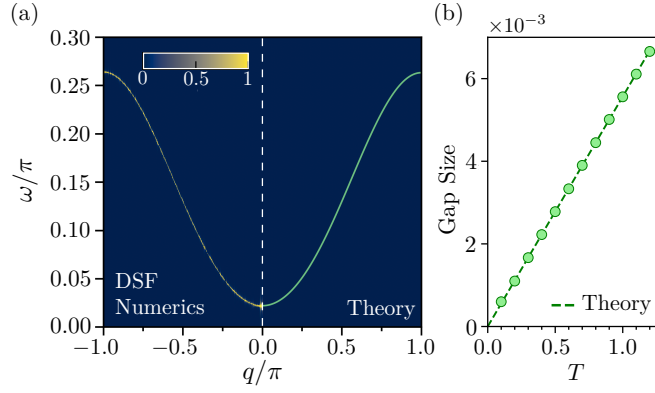


FIG. S7. (a) Dynamical structure factor through the first Brillouin zone for the 1D driven three-body interaction model, cf. Eq. (S.14). Fourier transformation is performed using $\ell = 10^4$ Floquet cycles. The left half displays the numerical results, while the right half shows the theoretical predictions. The dispersion spectrum follows the analytical prediction with a gap opened at $q=0$. The drive period is taken as $T=1$. (b) Linear dependence of ω versus T for the gap size. The system size $N=1000$ and the parameters $J_2=1$, $h_y=1$, $J_1=1$, $J_x=1$ are used for spin-dynamics simulation.

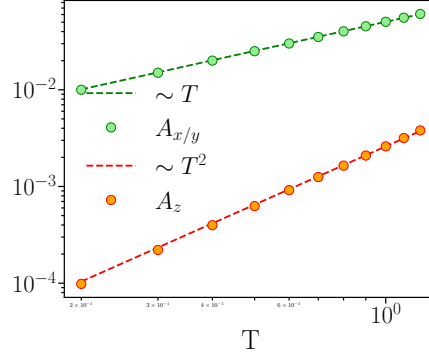


FIG. S8. 1D driven three-body interaction model, cf. Eq. (S.14): Scaling of oscillation amplitudes versus T . $A_{x/y} \propto T$ and $A_z \propto T^2$ are observed, suggesting that explicit symmetry breaking occurs hierarchically. The initial state is taken to be a spin wave state in the (x, y) -plane with $q=0.02\pi$, and $\theta_j = 0.02\pi$ for all spins. We use $N=1000$, $J_2=1$, $h_x=1$, $J_1=1$ and $J_x=1$.

closely mimics the Floquet results, confirming that $Q^{(1)}$ indeed dominates the damping of mNGs. For slightly larger drive period, the Floquet protocol generates a smaller linewidth, i.e., a longer lifetime. It essentially implies that $Q^{(2)}$ indeed stabilizes these mNGs, an counter intuitive observation since higher order terms normally speed up heating and hence shorten the lifetime of quasi-particles.

The linear dependence of the linewidth Γ and gap size Δ indicates that the ratio $\lambda \equiv \Gamma/\Delta$ is largely independent of T , and hence one cannot stabilize mNGs by increasing the driving frequency. However, one can still control this ratio by employing an initial ensemble with less spatial randomness, or at lower temperatures. To show this, we prepare the initial state ensemble as in the main text, and change θ to vary the spatial randomness. As shown in Fig. S9(b), the ratio λ can be systematically reduced upon using smaller spatial randomness. Therefore, the mNGs are well-defined quasi-particles given sufficiently low initial state temperature.

7. Ferromagnetic Quantum Spin Model

In the main text, we use a classical spin model to verify the existence of mNGs. However, the Floquet protocol equally applies to both quantum and classical systems. Therefore, we expect similar dynamical phenomena in the quantum system for the FM case. We verify the existence of magnon excitations by applying the protocol Eq. (1) to

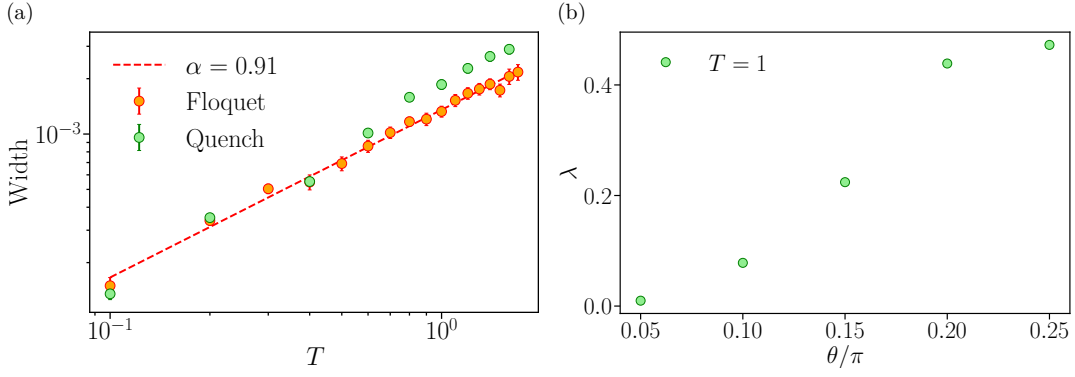


FIG. S9. 1D driven three-body interaction model, cf. Eq. (S.14): (a) The linewidth Γ exhibits a power-law scaling in the high-frequency regime with the exponent closing to 1. The results of the quenched protocol closely mimic the Floquet protocol in the high-frequency regime. Floquet protocol generates a smaller linewidth for large T . $\theta_j=0.1\pi$. (b) The monotonic dependence of λ on θ . The ratio λ can be suppressed by applying smaller spatial randomness. Various $\theta_j = \theta$ are used for characterizing the spatial randomness. We use $N=1000$, $T=1$, $J_2=1$, $h_x=1$, $J_1=1$ and $J_x=1$. 100 ensemble averages are performed with azimuthal angles ϕ_j randomly sampled within $(-\pi/3, \pi/3)$.

a quantum many-body system of spin- $\frac{1}{2}$, with the Hamiltonian

$$H_2 = -J_2 \sum_{j=1}^N \sigma_j^x \sigma_{j+1}^x + \sigma_j^y \sigma_{j+1}^y + \sigma_j^z \sigma_{j+1}^z, \quad H_1 = -h_x \sum_{j=1}^N \sigma_j^x, \quad H'_1 = -h_y \sum_{j=1}^N \sigma_j^y, \quad H_0 = J_x \sum_{j=1}^N \sigma_j^x \sigma_{j+1}^x, \quad (\text{S.19})$$

where we use Pauli operators.

We use Quspin [89] for numerical simulation and the system initially has all spins pointing up. Then we perform a single-site rotation on all spins around the x -axis by $e^{-i \sum_j \sigma_j^x \theta_j / 2}$, where the angle θ_j is chosen in a small range, yielding a sufficiently large magnetization density in z -direction and non-vanishing initial magnetization in the (x, y) -plane. The spatial randomness can mimic the thermal fluctuation that may exist in real quantum simulator platforms.

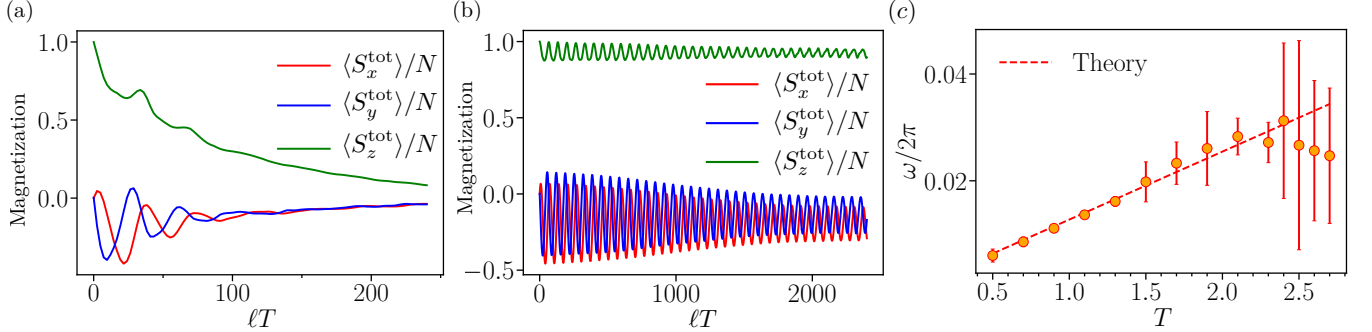


FIG. S10. (a) Dynamics of the total magnetization of the quantum spin chain, Eq. (S.19), with $T = 2.4$. Magnetization in the (x, y) -plane (red and blue) rotates at early times, and eventually decays. (b) Dynamics of the total magnetization with a smaller driving period $T = 1.2$. Persistent periodic rotation of magnetization in the (x, y) -plane (red and blue) confirms the existence of mNGs. (c) Linear dependence of the gap size versus T . We use a system of size $N = 20$ and parameters $J_2=1$, $h_x=2$, $h_y = -2$, $J_x=1$. We perform ensemble averages over 100 realizations where all spins rotate around the x -axis by $e^{-i \sum_j \sigma_j^x \frac{\theta_j}{2}}$ with θ_j randomly sampled within the range $(-\pi/100, \pi/100)$.

Fig. S10(a) and (b) illustrate the dynamics of total magnetization. The rotating magnetization around the z -axis (red and blue) confirms the presence of the mNG modes, which eventually damp out. The gap of the mode, corresponding to the oscillatory frequency of the magnetization, depends linearly on drive period T , as shown in Fig. S10(c). The theoretical calculation may fail for large T that fall outside the high frequency regime. These dynamical behaviors, analogous to those observed in the classical system, offer compelling evidence and support the validity of our analysis in the quantum system.

SM 3. MASSIVE NAMBU-GOLDSTONE MODES IN FLOQUET ANTI-FERROMAGNETIC SYSTEMS

We have provided a comprehensive analysis of FM in the main text, categorized as case 1. For case 2, we investigate the properties of the mNG modes in the Floquet system with AFM interaction, $J_2 < 0$. Significant distinctions between the two cases can be observed. For AFM, if we consider only the first two orders of the effective Hamiltonian, there exists a gapless Goldstone mode with linear dispersion and a gapped mNG with quadratic dispersion [66]. Taking higher-order terms into account, the gapless mode disappears and the spectrum of the gapped mode is slightly modified. The gap linearly depends on the drive period T in the high-frequency regime. Furthermore, we note that the stability of the gapped mode is quite different from the FM case.

1. Spin-wave Theory

We first derive the mNG properties theoretically, before showing the numerical verification. To begin with, we focus on the truncated Hamiltonian, Eq. (4), labeling $J \equiv J_2/5$ and the magnetic field strength along the z -direction by $h_z \equiv \frac{h_x h_y T}{200}$

$$Q_{\text{eff}} = -J \sum_j S_j^x S_{j+1}^x + S_j^y S_{j+1}^y + S_j^z S_{j+1}^z + h_z \sum_j S_j^z, \quad (\text{S.20})$$

where $J < 0$ for AFM interaction. If $h_z = 0$, there is one NG mode with linear dispersion. For non-zero h_z the ground state of the system features all spins having the same z -component with $S_j^z = \frac{h_z}{4J}$ and being antiparallel in (x, y) -plane for $|h_z| < -4J$. For $|h_z| > -4J$, the ground state is just the FM state along the z -axis. We focus on the former situation, since in our Floquet system the effective z -field strength linearly scales with T , which is a perturbatively small quantity. The Hamiltonian leads to the EOM

$$\begin{aligned} \dot{S}_j^x &= J[(S_{j-1}^z + S_{j+1}^z)S_j^y - (S_{j-1}^y + S_{j+1}^y)S_j^z] - h_z S_j^y, \\ \dot{S}_j^y &= J[(S_{j-1}^x + S_{j+1}^x)S_j^z - (S_{j-1}^z + S_{j+1}^z)S_j^x] + h_z S_j^x, \\ \dot{S}_j^z &= J[(S_{j-1}^y + S_{j+1}^y)S_j^x - (S_{j-1}^x + S_{j+1}^x)S_j^y]. \end{aligned} \quad (\text{S.21})$$

Without loss of generality, we assume that SSB happens in the x -direction. We linearize the EOM around the ground state by plugging $S_j^x = (-1)^j S_{\parallel} + \delta S_j^x$, $S_j^y = \delta S_j^y$ and $S_j^z = S_{\perp} + \delta S_j^z$ into Eq. (S.21) and keep terms up to the linear order of δS_j^{α} , where $\delta S_j^{\alpha} \ll 1$, $\alpha \in \{x, y, z\}$, $S_{\perp} = \frac{h_z}{4J}$ and $S_{\perp}^2 + S_{\parallel}^2 = 1$. Then we obtain

$$\begin{aligned} \delta \dot{S}_j^x &= \frac{h_z}{4} (2\delta S_j^y - \delta S_{j-1}^y - \delta S_{j+1}^y) - h_z \delta S_j^y, \\ \delta \dot{S}_j^y &= (-1)^{j+1} J S_{\parallel} (\delta S_{j-1}^z + \delta S_{j+1}^z + 2\delta S_j^z) + \frac{h_z}{4} (\delta S_{j-1}^x + \delta S_{j+1}^x - 2\delta S_j^x) + h_z \delta S_j^x, \\ \delta \dot{S}_j^z &= (-1)^j J S_{\parallel} (\delta S_{j-1}^y + \delta S_{j+1}^y + 2\delta S_j^y). \end{aligned} \quad (\text{S.22})$$

Note, since the ground state has two-site translation symmetry, we apply the Fourier transform to even and odd sites separately, $S_{j \in \text{even/odd}}^{\alpha} = \sum_q S_{e/o}^{\alpha}(q) e^{i(qa)j}$, $\alpha \in \{x, y, z\}$. For each q we can solve the linearized EOM analytically and obtain the dispersion relation

$$\begin{aligned} \omega_1 &= \pm \left| \sin \left(\frac{qa}{2} \right) \right| \sqrt{8J^2 S_{\parallel}^2 (\cos(qa) + 1) - \frac{h_z^2}{2} (\cos(qa) - 1)}, \\ \omega_2 &= \pm \cos \left(\frac{qa}{2} \right) \sqrt{\frac{h_z^2}{2} (\cos(qa) + 1) - 8J^2 S_{\parallel}^2 (\cos(qa) - 1)}, \end{aligned} \quad (\text{S.23})$$

where one is a gapless mode with linear dispersion $\omega_1 = \pm 2JS_{\parallel}|qa| + \mathcal{O}(|qa|^3)$ for small q , created by the SSB of $S_z^{\text{tot}} = \sum_j S_j^z$, while the explicit SB of $S_x^{\text{tot}} = \sum_j S_j^x$ and $S_y^{\text{tot}} = \sum_j S_j^y$ creates the gapped one with quadratic dispersion $\omega_2 = \pm h_z + \mathcal{O}(|qa|^2)$. The gap size equals the field strength, h_z , similar to the gapped mode in FM systems.

In principle, linearization can be carried out through different methods. Here, we present an alternative way to derive the dispersion for AFM which leads to the same dispersion. We parameterize the spin variables as $S_j^x = \sin \theta_j \cos \phi_j$,

$S_j^x = \sin \theta_j \sin \phi_j$, $S_j^y = \cos \theta_j$, and linearize the EOM of θ and ϕ to leading order

$$\begin{aligned}\delta \dot{\theta}_j &= J \sin \theta_0 (\delta \phi_{j-1} + \delta \phi_{j+1} - 2\delta \phi_j), \\ \delta \dot{\phi}_j &= \frac{J_2}{\sin \theta_0} [2\delta \theta_j - \cos 2\theta_0 (\delta \theta_{j+1} + \delta \theta_{j-1})],\end{aligned}\quad (\text{S.24})$$

where $\cos \theta_0 = h_z/4J$. This EOM can be solved by performing the Fourier transform to the angle variables $\delta \theta_{j \in \text{even/odd}} = \sum_q \delta \theta_{e/o}(q) e^{i(qa)j}$ and $\delta \phi_{j \in \text{even/odd}} = \sum_q \delta \phi_{e/o}(q) e^{i(qa)j}$, leading to two modes

$$\begin{aligned}\omega'_1 &= \pm \left| \sin \left(\frac{qa}{2} \right) \right| \sqrt{8J^2(1 - \cos 2\theta_0 \cos qa)}, \\ \omega'_2 &= \pm \cos \left(\frac{qa}{2} \right) \sqrt{8J^2(1 + \cos 2\theta_0 \cos qa)},\end{aligned}\quad (\text{S.25})$$

which reproduce the result Eq. (S.23).

2. Numerical Verification of Massive Goldstone Modes

Here we certify the mNGs via numerical simulation. The AFM ground state of the Hamiltonian Eq. (S.20) can be formulated as

$$\cos \theta_j = -\frac{h_x h_y T}{160 J_2}, \text{ for all } j; \quad \phi_j = 0, \text{ for } j \in \text{even}, \phi_j = \pi, \text{ for } j \in \text{odd}. \quad (\text{S.26})$$

We prepare the initial state as follows: first, the system is initialized as all spins deviate from the z -axis by a small angle $\delta \theta_j = 0.01\pi$ and $\delta \phi_j$ are randomly sampled within the range $(-\pi/3, \pi/3)$; then all spins are rotated by θ_j and ϕ_j in Eq. (S.26). In this way, we generate the initial ensemble with spatial randomness on top of the ground state.

To verify Eq. (S.23), we first simulate the quenched dynamics with the time-independent Hamiltonian Eq. (S.20). Numerically we integrate the EOM Eq. (S.21) via the standard Runge-Kutta method. The DSF computed through the first Brillouin zone is shown in Fig. S11 (a): numerically we observe two modes (dashed lines on the left side of panel (a)) that match well with our theoretical prediction (solid lines on the right side). A mNG gap opens at $q = 0$ corresponding to the oscillatory frequency of the total magnetization.

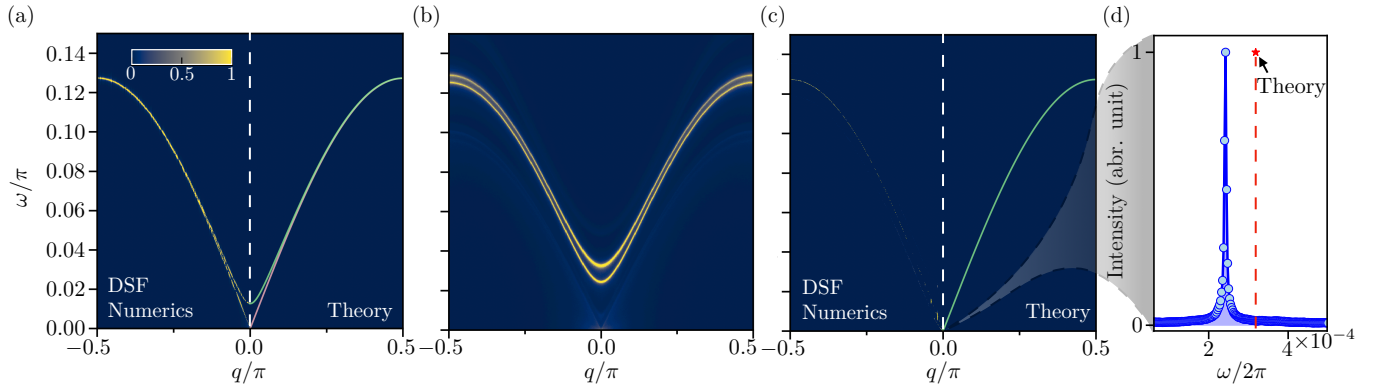


FIG. S11. Dynamical structure factor (DSF) through the Brillouin zone of AFM model. (a) Obtained from spin-dynamics simulation of a time-independent Hamiltonian, Eq. (S.20), with parameters $J=-1/5$, $h_z=1/25$. A gapped mode with quadratic dispersion and a gapless mode with linear dispersion appear in accordance with the theoretical prediction. (b) Floquet spin-dynamics simulation with $T=2$, $J_2=-1$, $h_x=2$, $h_y=2$ and $J_x=1$, which gives the same parameters as (a). However, this spectrum is very different from (a) due to significant higher-order perturbations that are not involved in Q_{eff} . Fourier transformation is performed by using $\ell=10^4$ Floquet cycles. (c) Obtained from spin-dynamics simulation of Eq. (3) with $T=0.4$, $J_2=-1$, $h_x=1$, $h_y=1$ and $J_x=1$. The gapped mode still matches our theory, while the gapless mode disappears. Fourier transformation is performed by using $\ell=5 \times 10^4$ Floquet cycles. The Fourier density of $q = 0$ is illustrated in (d), where the gap is clearly visible. System size is $N = 1000$. Ensemble averaging over 100 realizations is performed with $\delta \theta_j = 0.01\pi$ and $\delta \phi_j$ randomly sampled within $(-\pi/3, \pi/3)$ for (a) and (b), while $\delta \phi_j$ randomly sampled within $(-\pi/6, \pi/6)$ for (c).

For the Floquet system, drive-induced higher-order terms break the $O(2)$ symmetry, and hence the ground state degeneracy is lifted. Therefore, we have to find the ground state of the effective Hamiltonian $\tilde{Q}_{\text{eff}} = Q^{(0)} + Q^{(1)} + Q^{(2)}$

truncated at order $\mathcal{O}(T^2)$. $Q^{(2)}$ takes a complicated form

$$\begin{aligned}
Q^{(2)} &= \frac{T^2}{4000} ([H_0 + H_1 + H'_1, [H_1, H'_1]] - [2H_1 - 2H_2 + H'_1, [H_2, H_1]] + 2[[H_0, H_1 + H'_1], H_2] - [3H_1 - 2H_2 + 2H'_1, [H_2, H'_1]]), \\
&= -\frac{T^2}{4000} \sum_j h_x h_y (h_x S_j^y - h_y S_j^x) - J_x h_x h_y S_j^y (S_{j+1}^x + S_{j-1}^x) + 2J_x h_y J_2 [S_j^y (S_{j+1}^x + S_{j-1}^x)^2 \\
&\quad - (S_{j+1}^x + S_{j-1}^x) S_j^x (S_{j+1}^y + S_{j-1}^y) + (S_{j+1}^z + S_{j-1}^z) S_j^z (S_{j+1}^y + S_{j-1}^y) - (S_{j+1}^z + S_{j-1}^z) S_j^y (S_{j+1}^z + S_{j-1}^z)],
\end{aligned} \tag{S.27}$$

and determining analytically its effect on the ground state is quite cumbersome. Instead, we numerically minimize the energy \tilde{Q}_{eff} , by constraining the optimization parameter space within the state manifold with 2-site translation invariance. Note, the optimized state may not be exact but should be close to the true ground state of \tilde{Q}_{eff} . Also, the optimized state reduces to the AFM ground state Eq. (S.26), analytically obtained for $Q^{(0)} + Q^{(1)}$, if we neglect the effect of $Q^{(2)}$. A small deviation from this state appears as T increases. This optimization is not necessary for detecting the mNGs, as long as T is sufficiently small. However, this optimization can generate a clearer signal of DSF as shown in Fig. S11.

We now simulate the Floquet protocol that generates the effective Hamiltonian Eq. (S.20), with the same parameters as used in Fig. S11(a). Similarly, we introduce randomness to the optimized state, and obtain the DSF as shown in Fig. S11(b). The spectrum is drastically different from panel (a). This happens because, in order to match the Hamiltonian parameters we use a large drive period T , which causes non-negligible higher-order effects. In Fig. S11(c) we use a higher driving frequency to suppress these higher order effects, and as shown in panel (d) one mNG mode appears with a finite gap opened at $q = 0$. We compare these numerical results with our theoretical prediction (red) in panel (d), where a small deviation appears. As shown in Fig. S12(a), this discrepancy can be systematically suppressed by reducing the drive period.

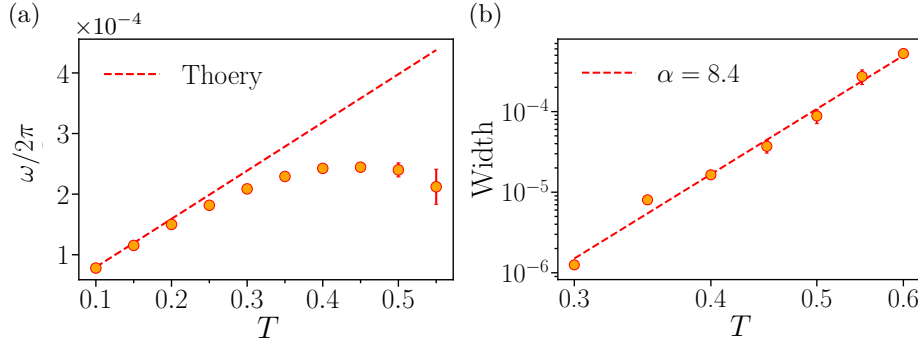


FIG. S12. (a) Linear dependence of ω versus T for the gap size. Deviation between the numerical and theoretical results reduces for higher driving frequencies. (b) The width Γ exhibits a power-law scaling in the high frequency regime with the scaling exponent $\alpha \approx 8$. We use $N = 1000$, $J_2 = -1$, $h_x = 1$, $h_y = 1$ and $J_x = 1$. Ensemble averaging over 100 realizations is performed with $\delta\theta_j = 0.01\pi$ and $\delta\phi_j$ randomly sampled within the range $(-\pi/6, \pi/6)$.

In Fig. S12(b), we plot the linewidth Γ for $q = 0$ by performing Fourier transform to the dynamics of total magnetizations over time, for varying T . The linewidth is determined by averaging the full-width at 10%, 15%, and 20% of the maximum intensity of the Fourier peak, with their standard deviation serving as the error bar. Interestingly, Γ exhibits a power-law scaling T^α with a large scaling exponent $\alpha \approx 8$, suggesting that the lifetime of the mNG mode can be notably changed by slightly tuning the driving frequency.

We also note that the gapless NG mode no longer exists in the current Floquet setting, implying that its robustness is worse than the gapped mNGs. It remains an interesting and open question how to stabilize gapless modes in Floquet systems.

SM 4. TROTTERIZED SIMULATION PROTOCOL

To achieve an efficient long-time simulation of the classical spin dynamics, we use the Trotterization method for the evolution of the Heisenberg model $H = -J \sum_j \mathbf{S}_j \cdot \mathbf{S}_{j+1}$. We decompose H into $H_e = -J \sum_{j \in \text{even}} \mathbf{S}_j \cdot \mathbf{S}_{j+1}$ and $H_o = -J \sum_{j \in \text{odd}} \mathbf{S}_j \cdot \mathbf{S}_{j+1}$, where the summation is performed over either even or odd sites. Note, we do not

use Trotter decomposition for H_1 and H'_1 in the system discussed in Sec. SM 26. There, the Hamiltonian contains three-body interactions for which one can not easily integrate the EOM analytically over a certain time window.

The EOMs generated by the two Hamiltonians can be analytically integrated over the driving duration t , leading to the update maps

$$\tau_e(\vec{S}_{j(j+1)}) = \frac{1}{k_2^2} \begin{pmatrix} [B_1^2 + (B_2^2 + B_3^2) \cos(J_2^j k_2 t)] S_{j(j+1)}^x \\ + [B_1 B_2 (1 - \cos(J_2^j k_2 t)) + k_2 B_3 \sin(J_2^j k_2 t)] S_{j(j+1)}^y \\ + [B_1 B_3 (1 - \cos(J_2^j k_2 t)) - k_2 B_2 \sin(J_2^j k_2 t)] S_{j(j+1)}^z \\ [B_1 B_2 (1 - \cos(J_2^j k_2 t)) - k_2 B_3 \sin(J_2^j k_2 t)] S_{j(j+1)}^x \\ + [B_2^2 + (B_1^2 + B_3^2) \cos(J_2^j k_2 t)] S_{j(j+1)}^y \\ + [B_2 B_3 (1 - \cos(J_2^j k_2 t)) + k_2 B_1 \sin(J_2^j k_2 t)] S_{j(j+1)}^z \\ [B_1 B_3 (1 - \cos(J_2^j k_2 t)) + k_2 B_2 \sin(J_2^j k_2 t)] S_{j(j+1)}^x \\ + [B_2 B_3 (1 - \cos(J_2^j k_2 t)) - k_2 B_1 \sin(J_2^j k_2 t)] S_{j(j+1)}^y \\ + [B_3^2 + (B_1^2 + B_2^2) \cos(J_2^j k_2 t)] S_{j(j+1)}^z \end{pmatrix}, \quad (\text{S.28})$$

for H_e , $j \in \text{even}$, and

$$\tau_o(\vec{S}_{j(j+1)}) = \frac{1}{k_2^2} \begin{pmatrix} [B_1^2 + (B_2^2 + B_3^2) \cos(J_2^j k_2 t)] S_{j(j+1)}^x \\ + [B_1 B_2 (1 - \cos(J_2^j k_2 t)) + k_2 B_3 \sin(J_2^j k_2 t)] S_{j(j+1)}^y \\ + [B_1 B_3 (1 - \cos(J_2^j k_2 t)) - k_2 B_2 \sin(J_2^j k_2 t)] S_{j(j+1)}^z \\ [B_1 B_2 (1 - \cos(J_2^j k_2 t)) - k_2 B_3 \sin(J_2^j k_2 t)] S_{j(j+1)}^x \\ + [B_2^2 + (B_1^2 + B_3^2) \cos(J_2^j k_2 t)] S_{j(j+1)}^y \\ + [B_2 B_3 (1 - \cos(J_2^j k_2 t)) + k_2 B_1 \sin(J_2^j k_2 t)] S_{j(j+1)}^z \\ [B_1 B_3 (1 - \cos(J_2^j k_2 t)) + k_2 B_2 \sin(J_2^j k_2 t)] S_{j(j+1)}^x \\ + [B_2 B_3 (1 - \cos(J_2^j k_2 t)) - k_2 B_1 \sin(J_2^j k_2 t)] S_{j(j+1)}^y \\ + [B_3^2 + (B_1^2 + B_2^2) \cos(J_2^j k_2 t)] S_{j(j+1)}^z \end{pmatrix}, \quad (\text{S.29})$$

for H_o , $j \in \text{odd}$, where the average fields originating from the neighboring sites read $B_1 = S_j^x + S_{j+1}^x$, $B_2 = S_j^y + S_{j+1}^y$, $B_3 = S_j^z + S_{j+1}^z$, and $k_2 = B_1^2 + B_2^2 + B_3^2$.

We use the following protocol to generate the spin dynamics (second-order Suzuki-Trotter decomposition)

$$H_{\text{Trotter}}(t) = \begin{cases} H_e & \text{for } t \in [0, \frac{T}{4}], \\ H_o & \text{for } t \in [\frac{T}{4}, \frac{3}{4}T], \\ H_e & \text{for } t \in [\frac{3}{4}T, T]. \end{cases} \quad (\text{S.30})$$

Time evolution after a full period can be effectively described by a Hamiltonian \tilde{H} . One can prove that $\tilde{H} = H + \mathcal{O}(T^2)$ using an inverse-frequency expansion, indicating that the error of this approximation is introduced at the order $\mathcal{O}(T^2)$. When we apply it to the whole protocol Eq. (1) to approximate the Heisenberg Hamiltonian, it does not change the form of Q_{eff} , Eq. (2) as well as the gap size of mNGs. Indeed, in principle, we can further suppress the simulation error to any required order by using higher-order Trotterization method, if needed.